Category: Original article

Deciphering the pressure–temperature path in low-grade metamorphic rocks by combining crystal chemistry, thermobarometry and thermodynamic modelling: an example in the Marguareis Massif (Western Ligurian Alps, Italy)

Short Title: Pressure–Temperature path of low-grade metamorphic rocks revealed by integrating quantitative and qualitative approaches

Edoardo Sanità[1], Maria Di Rosa[1], Jean-Marc Lardeaux[2,3], Michele Marroni[1,4*], Marco Tamponi[1], Marco Lezzerini[1], Luca Pandolfi[1]

[1] Università di Pisa, Dipartimento di Scienze della Terra, Via Santa Maria, 53, Pisa, Italia

[2] UMR Géosciences Azur, Université de la Côte d'Azur, Nice-Sophia Antipolis, France

[3] Czech Geological Survey, Centre for Lithospheric Research, Klárov 3, Prague 1, 118 21, Czech Republic

[4] Consiglio Nazionale della Ricerca, Istituto di Geoscienze e Georisorse, IGG-CNR, Via Moruzzi, 1 Pisa, Italia

ORCID

Edoardo Sanità: 0000-0002-5488-9832; Maria Di Rosa: 0000-0002-1154-7429; Jean Marc Lardeaux: 0000-0001-7666-7109; Michele Marroni: 0000-0002-2947-3739; Marco Tamponi: 0000-0003-3218-0512; Marco Lezzerini: 0000-0001-9204-4462; Luca Pandolfi: 0000-0002-6129-647X

*Corresponding author: Prof. Michele Marroni, e-mail: michele.marroni@unipi.it

This is a 'preproof' accepted article for Mineralogical Magazine. This version may be subject to change during the production process.
DOI: 10.1180/mgm.2024.80

phone: +39 333 6056704

Abstract

Unveiling the pressure–temperature path of low-grade metamorphic rocks is challenging because of the occurrence of detrital minerals phases and high-variance mineral assemblages (*i.e.*, chlorite–white mica–quartz). This paper offers an attempt to reconstruct the pressure–temperature history on metapelites from a low-grade metamorphic unit, *i.e.*, the Cabanaira Unit, located in the Marguareis Massif (Western Ligurian Alps, Italy). In order to obtain the most robust result possible, multiequilibrium thermobarometry, forward modelling and crystallochemical indexes measurement are used together to reconstruct a pressure–temperature path, considering strengths and weaknesses of each of these methods.

This multidisciplinary approach allowed us to reconstruct the metamorphic evolution of the unit of interest, characterized by a pressure peak achieved under low-temperature conditions (0.85-0.68 GPa and 250-285 °C) followed by decompressional warming (low pressure–high temperature, 0.4-0.6 GPa and 300-335 °C).

This pressure–temperature path is consistent with the tectonic evolution of the investigated area proposed by previous authors, where a geological scenario in which the Cabanaira Unit experienced subduction-related processes was postulated, even if the reasons for warming remain unclear.

Multiequilibrium thermobarometry is considered to be the most suitable method to unravel the metamorphic history of low-grade rocks, while forward thermodynamic modelling and the calculation of crystallochemical indexes seem to resolve only some segments of the pressure–temperature path.

https://doi.org/10.1180/mgm.2024.80 Published online by Cambridge University Press

Keywords: Low-grade rocks, thermobarometry, crystallochemical indexes, thermodynamic modelling, Marguareis Massif, Southwestern Alps.

1. Introduction

In recent decades, the quantification of intensive parameters of metamorphism has undergone remarkable evolution with the production of internally consistent thermodynamic databases (Berman, 1988; Holland and Powell, 1998; 2011) and the improvement of our understanding of mixing properties and activity–composition relationships for mineral solid solutions and melts (e.g., Green et al., 2016; White et al., 2014). The development of software using these various databases has had a significant impact on modelling the thermodynamic evolution of metamorphic rocks (Powell et al., 1998; Connolly, 2005; De Capitani and Petrakakis, 2010; Duesterhoeft and Lanari, 2020; Xiang and Connolly, 2021). These approaches allow the stability fields, mode and composition of minerals to be estimated for a given rock composition in the pressure–temperature (*P–T*) space (Thinkam and Ghent, 2005; Powell et al., 2005; Spear et al., 2016; Lanari and Duesterhoeft, 2019; Lanari et al., 2019). This, together with decisive progress in "in situ" geochronology has allowed better understanding of the tectono-metamorphic evolution of high-grade units. (*i.e.,* Štípská et al., 2006, 2019; Plunder et al., 2012; Airaghi et al., 2017; Tedeschi et al., 2017; Luoni et al., 2019; Lotout et al., 2020; Ghignone et al., 2021; Bonnet et al., 2022; Collett et al., 2022). In contrast, poor thermomechanical constraints on the tectonic evolution of low- and very low-grade metamorphic units involved in external collision zones were implemented (e.g., Muirhead et al., 2020 and quoted references; Willner, 2021). Currently, electron probe microanalysis (EPMA) provides high-quality reliable and reproducible chemical analysis, even on fine-grained minerals that are largely present in low-grade metamorphic rocks (*i.e.*, see Lanari et al., 2012; Airaghi et al., 2017; Di Rosa et al., 2019;

https://doi.org/10.1180/mgm.2024.80 Published online by Cambridge University Press

Sanità et al., 2022b; 2022c; Barbero et al., 2023). This has led metamorphic petrologists to investigate a larger dataset of metasedimentary rocks, opening new scenarios for understanding low-grade metamorphism based on robust *P–T* estimations (*i.e.*, Massonne and Schreyer, 1987; Vidal et al., 1999; Vidal and Parra, 2000; Parra et al., 2002; Agard et al., 2001; Vidal et al., 2005; Dubacq et al., 2010; Pourteau et al., 2014; Lanari et al., 2014; Bourdelle and Cathelineau, 2015). Among metasedimentary rocks, metapelites are widely represented lithotypes in mountain belts. The difficulty in studying this kind of metamorphic rock is related to the occurrence of detrital minerals, which remain as relict phases without reacting during metamorphism, thus making the reactive bulk composition difficult to investigate (*i.e.,* Tracy, 1982; Marmo et al., 2002; Tinkham and Ghent, 2005; Lanari and Engi, 2017). Therefore, a combination of careful microstructural investigations and various thermodynamic methods and are required to constrain the *P–T* paths recorded by these rocks. In this study, we present an attempt to reconstruct a *P–T* path by combining crystallochemical indexes and thermodynamic modelling including multiequilibrium thermobarometry and phase equilibria relationships (*i.e.*, pseudosections). This approach is tested in metapelites sampled in a low-grade unit, *i.e.*, the Cabanaira Unit, located in the High Valle Roja in the southwestern sector of the Marguareis Massif along the Italian–French border (Western Ligurian Alps, Figure 1). The reconstructed *P–T* path is then discussed to evaluate its consistency with respect to the available regional tectonic framework of the investigated area.

2. Geology of the sampling area

The studied samples were collected in the Cabanaira area within the Marguareis Massif. This massif is located along the Western Ligurian Alps which are part of the southwestern prolongation of the Alpine collisional belt (Figure 1a, b). The latter is characterized by a long-lived convergence history between the Europe and Adria Plates (*e.g.*, Handy et al., 2010; Schmid et al., 2017; Manatschal et al., 2022). This history started in the Late Cretaceous with a subduction system leading to progressive consumption of the Ligure–Piemontese Ocean (ocean subduction stage), which was interposed

https://doi.org/10.1180/mgm.2024.80 Published online by Cambridge University Press

between the two plates (*e.g.,* Stampfli et al., 2001; Beltrando et al.; 2010; Lardeaux, 2014; Lagabrielle et al., 2015; Marotta et al., 2018; Roda et al., 2019), and part of the Adria Plate (*e.g.,* Polino et al., 1990; Lardeaux and Spalla, 1991; Stöckhert and Gerya, 2005). Subsequently, after the closure of the Ligure–Piemontese Ocean, the European continental crust started to be involved in a subduction system (continental subduction stage, Rosenbaum et al., 2002; Handy et al., 2010; Schmid et al., 2017) in the Eocene until continental collision occurred during the early Oligocene (collision stage, Ford et al., 2006; Simon-Labric et al., 2009). Finally tectonic denudation started during Miocene (Tricart et al., 2001).

According to the classic tectonic framework proposed for the southwestern Alps (Vanossi et al., 1984; Seno et al., 2005; Seno et al., 2003; Bonini et al., 2010; Mueller et al., 2020), their westernmost part (outer sectors) is characterized by a SW-verging fold-and-thrust belt consisting of the Dauphinois/Provençal Units, which, together with the External Crystalline Massifs, represent the former European continental margin poorly involved in the Alpine collisional stage. These units are separated by the southern prolongation of the Penninic Front, whose activity is constrained at 33 Ma in this sector of the belt (Maino et al., 2015), from the Briançonnais Units (Figure 1a, see Sanità et al., 2021, 2023). The latter, together with the Internal Crystalline Massifs (blue domains of Figure 1a), are classically regarded as the thinned portion of the European continental margin that was deeply involved in continental subduction, which is largely documented in the whole Western Alps (*i.e.,* Michard et al., 2004; Bousquet et al., 2008; Lanari et al., 2012; Sterzynsky et al., 2011; Groppo et al., 2019; Manzotti et al., 2022; Sanità et al., 2022b). They are thrust in turn by oceanic-derived units representative of the Ligure–Piemontese Ocean (*i.e.*, the Moglio-Testico and the Borghetto d'Arroscia Units, Vanossi et al., 1984; Di Giulio, 1988; Di Giulio, 1992; Mueller et al., 2020; Sanità et al., 2022c; and the Voltri Group, Chiesa et al., 1975; Capponi and Crispini, 2002; Capponi et al., 2009). The San Remo-Monte Saccarello Unit, whose paleogeographic origin is a matter of debate (Sagri, 1984; Mueller et al., 2018; Sanità et al., 2020; Sanità, 2023), forms the uppermost portion of the tectonic pile (Figure 1a, b, c, see also Maino and Seno, 2016 and Mueller et al., 2020). Moving

https://doi.org/10.1180/mgm.2024.80 Published online by Cambridge University Press

towards the Ligurian Sea, the San Remo-Monte Saccarello Unit tectonically overlays the Dauphinois/Provençal Units (Figure 1a, b, c see also Perotti et al., 2012; Decarlis et al., 2014; Mueller et al., 2020).

In the sampling area, the Cabanaira Unit (cf. Roja Unit of Piana et al., 2014 and Rocca-Borbone Unit of Maino and Seno, 2016) is separated, to east, by the Penninic Front from a SW-verging stack of units (according to Sanità et al., 2020; 2021, Figures 1b, d). The latter, from the upper to the lower structural levels, consists of i) the topmost Marguareis Unit (Briançonnais Domain), regarded as a fragment of the European continental margin involved in the subduction zone (Carminati, 2001; Decarlis et al., 2013; Sanità et al., 2020; 2021) that experienced high pressure-low temperature (*HP–LT)* metamorphism (1.0-0.9 GPa and 280-330 °C Sanità et al., 2022b); ii) the Helminthoid Flysch Unit (cf. San Remo-Monte Saccarello Unit of Sagri, 1984), which is here considered as being derived from the External Ligurian Domain (according to Sanità et al., 2020; 2022a; Sanità, 2023) and showing diagenetic/anchizone-type metamorphic imprint (*T* never exceeding 220 °C, Piana et al., 2014; Maino et al., 2020 - and *P* in the range of 0.5-0.2 GPa, Sanità, 2023). To the southeast, the oceanic-derived Moglio-Testico Unit crops out (Figure 1d), and it is tectonically located between the Marguareis Unit and the Helminthoid Flysch showing an *HP* metamorphic imprint achieved during the oceanic subduction stage (1.2-1.0 GPa and 260-330 °C, Sanità et al., 2022c).

According to Sanità et al. (2020), the Cabanaira Unit (Figure 2a) consists of a Jurassic platform meta-carbonate (Forte Pepin Limestone, FPL) unconformably underlying the middle Eocene (Gidon, 1972) *Nummulites*-rich meta-limestones (Nummulitic Limestone, NUM) and foredeep meta-turbidites (Cima Aurusi Formation, CAF). The finite strain pattern of the Cabanaira Unit, which records the superposition of folding and thrusting events (Sanità et al., 2020; 2021), is thought to be the result of its involvement in alpine convergent-related processes. The oldest deformation event (here D1 phase, cf. $D1_{CU}$ *pre-stacking structures* of Sanità et al., 2020) produced an SW-verging folding system that was confined within the unit and developed from micro- to map-scale (Figures 2b, 3a). The associated axial planes were cut by the subsequent deformation event (*syn-stacking event* of Sanità et al., 2020),

https://doi.org/10.1180/mgm.2024.80 Published online by Cambridge University Press

which was responsible for the thrusting of the Helminthoid Flysch Unit onto the already deformed Cabanaira Unit (see geological cross-section of Figure 2b). The last deformation events are represented by a fold system (here called the D2 phase, cf. *post-stacking folds* of Sanità et al., 2020) with roughly flat-lying axial planes and high-angle faults. D1-related folding produced isoclinal to tight F1 folds that are associated with S1 tectonic foliation (Figure 2b, 3a). At the outcrop scale, this foliation is a continuous surface that is well developed in fine-grained rocks (*i.e.*, metapelites), while in the more competent layers (*i.e.*, limestones), it appears as a spaced cleavage or, as in other cases, it is scarcely preserved.

3. Materials and methods

3.1 Materials

To perform this study, we collected samples where the S1 foliation is well preserved, *i.e.*, the metapelites from the topmost deposits (Cima Aurusi Formation) of the Cabanaira Unit. In these specimens, the S1 foliation is a slaty cleavage developed by pressure solution processes (i.e. pressure solution creep) diagnostic for fluids-assisted deformation under low-temperature conditions (Rutter, 1983; Gratier et al. 2013 with references therein). Parallel to this dissolution schistosity plane white mica (Wm), chlorite (Chl) and quartz (Qz) (mineral abbreviations after Warr, 2021 with the exception of white mica) with marked shape preferred orientation are often well developed. Moreover, ultra-local micro-domains where grains of Wm + Chl + Qz ± calcite (Cc) and potassic feldspar (K-Fsp) can be observed (Figure 3b, c, d) showing clear textural equilibrium relationships suggesting that metamorphic crystallization of new grains occurred along the S1 foliation. Along the S1 foliation, syn-metamorphic elongated Wm grains show lengths never exceeding 15-25 µm (Figures 3b, c, d, e), while Chl grains are stubby, sometimes with recrystallized tails, reaching up to 30 µm in size (Figures 3b, c, d, e). Both show undulose extinction and sharp edges with apparently no evidence of chemical zoning (Figures 3b, c). Large and altered Wm and Chl crystals (both more than 60 µm in length)

https://doi.org/10.1180/mgm.2024.80 Published online by Cambridge University Press

showing frayed edges and slight chemical zoning are also present (Figures 3e) whose micro-textures suggest a detrital origin. The latter are mostly set along the primary bedding (S0 in Figures 3d, e) and show clear cross-cutting relationships with the syn-metamorphic mineral growth along the S1 foliation (Figures 3d, e). Plagioclase (albite?, Figure 3c) are also present and they are characterized by stubby grains with frayed edges wrapped by very fine-grained crystals of Wm and Chl and indicating a detrital nature. According with the above microstructural observations the main deformation mechanisms include re-crystallization, pressure solution and passive rotation of detrital phyllosilicates (according to Groshong, 1988; Hirt and Tullis, 1992; Paschier and Trouw, 2005).

3.2 Methodological approach

Microstructures and micro-textures were the main criteria used to select the microdomains characterized by dynamic recrystallization of Wm and Chl with which the *P* and *T* conditions were estimated (white box of Figure 3e, see also the next section). Figure 3e shows the micro-area (orange box in Figure 3d) chosen to perform the *P–T* investigation. The microdomain of Figure 3d (whose close-up are represented by the X-ray maps of the Figures 4a, b) was chosen in order to include neo-formed grains of Chl and Wm and Qz, which grew along the S1 foliation, avoiding those detrital (Figures 3d, e). In the selected micro-area, syn-metamorphic Chl and Wm (white box of Figure 3e) are slightly zoned with rims slightly brighter than cores. Wm and Chl grains occur either as well-defined grains or very fine-grained crystals.

As the detrital minerals cannot be excluded as relict phases in the micro-domain of interest and because of the high-variance Chl–Wm–Qz mineral assemblage, different analytical techniques, including inverse multiequilibrium thermobarometry and forward modelling (*i.e.*, pseudosections) and Wm "crystallinity" index (WmIC) and b_0 cell parameters were used. Eleven samples of metapelites (Figure 2a, the geographic coordinates of each sample are available in the T1 table in supplementary materials S1) were selected to perform the measurements. Thermobarometric estimates and forward modelling were performed using X-ray compositional maps on one sample of

https://doi.org/10.1180/mgm.2024.80 Published online by Cambridge University Press

metapelite collected in the F1 hinge zone (sample ED208a), while the WmIC were measured on 10 samples of carbonate-free metapelites powders (ED203-208 and ED2017-220). The WmIC (Kubler, 1967a, b) and the b_0 cell parameter (Guidotti and Sassi, 1986; Guidotti et al., 1989; Franceschelli et al., 1989) are largely known as qualitative methods and are thought to be functions of *T* and *P*, respectively. In this work, the *T* and *P* ranges obtained with WmIC and b_0 cell parameter were compared with the results of the other independent methods applied (Guidotti and Sassi, 1998; Kubler and Goy-Eggenberger, 2001; Abad and Nieto, 2007; Warr and Ferreiro Mählmann, 2015).

3.2.1 X-ray map processing and local bulk composition

The X-ray map was obtained using a JEOL 8800 electron microprobe at the Dipartimento di Scienze della Terra "A. Desio" (Milano, Italy), equipped with five wavelength-dispersive spectrometers and calibrated with the following standards: wollastonite (Ca, Si), orthoclase (K), albite (Al), periclase (Mg), rhodonite (Mn), TiO_2 (Ti), Al_2O_3 (Al), Fe_2O_3 (Fe) and Cr_2O_3 (Cr) (for the acquisition settings see supplementary material S2, while see tables T2 and T3 in supplementary material S2 and Figure F1 for the position of each spot analysis within the investigated micro-area). The X-ray intensities were processed with XMapTools 3.2 software (Lanari et al., 2014c) to get oxide composition (wt. %) quantitative map using the spot analyses (see T2 and T3 tables in S2 for criteria used to evaluate the quality of standard analysis) as internal standard following the procedure described by De Andrade et al. (2006). The Local bulk Composition (LBC) of the selected micro-area (white box of Figure 3e) was obtained using the *density-corrected oxide map* function implemented in XMapTools program (see the supplementary materials S2 for details about the adopted procedure).

3.2.2 Forward modelling

https://doi.org/10.1180/mgm.2024.80 Published online by Cambridge University Press

A forward phase equilibria modelling was performed in order to evaluate the equilibrium of the metamorphic minerals grew along the S1 foliation using the LBC extrapolated from the wt.% map (e.g., Lanari and Engi, 2017, see table T4 in supplementary material S3). The Gibbs free energy minimization algorithm of Theriak-Domino (de Capitani and Brown, 1987; de Capitani and Petrakakis, 2010), was used to compute isochemical phase diagrams and mineral compositional isopleths of Wm and Chl with or without the ferric iron content. The internally consistent thermodynamic database *JUN92.bs* (Berman, 1988; Pourteau et al., 2014) implemented with the solution models of Parra et al. (2002) with the revised Margules parameters for Wm (Dubacq et al., 2010), Chl (Vidal et al., 2005), carpholite (solution models of Vidal et al., 1992; Dubacq, 2008) and chloritoid (solution models of Vidal et al., 2001) were used to perform all of the computations (see the supplementary material S3 for details about the solution models included in the database) with an excess of H_2O-rich fluid (aH_2O=0.8).

3.2.3 Thermobarometry

Multi-equilibrium modelling approach for partially re-equilibrated (this study) allows us to detect different segments of the *P–T* path (*i.e.*, peak *P*, peak *T*; according with Lanari and Duesterofth, 2019). Therefore, to estimate the *P* and *T* conditions recorded by the Cabanaira Unit, chemical analyses of Chl and Wm grains grown along the S1 foliation were processed with three different methods using ChlMicaEqui software (Lanari, 2012), which operates assuming the presence of water (H_2O) and Qz within the assemblage. In the calibrated compositional map (e.g., Figure 4a), we investigated the micro-area where the relationships between the identified S1 foliation and the primary bedding (white box of in Figure 3e) were unambiguously clear. In this microdomain, we considered all chemical heterogeneity of Chl and Wm using XMapTools software (Lanari et al., 2014a). This operation allowed us to investigate chemical analyses for each neo-formed mineral phase (Chl and Wm) avoiding the detrital crystals (see Table 1, 2). The methods used to retrieve the *P–T* equilibrium conditions are the Chl-Qz-H_2O, the Phg-Qz-H_2O and the Chl-Phg-Qz-H_2O methods.

https://doi.org/10.1180/mgm.2024.80 Published online by Cambridge University Press

The Chl-Qz- H_2O method (Vidal et al., 2006) has been used to calculate the temperature range of chlorite formation (see supplementary material S4 for more details about this geothermometer), with an equilibrium tolerance of 30 °C estimating the percentage of Fe^{3+} for each Chl analysis fixing the pressure value (see F2 in supplementary S4) and specific water activity (0.8 for the presence of Cc, according to Frassi et al., 2022).

Phg-Qz-H_2O method (Dubacq et al., 2010) rely on the de-hydration of Wm, to refine the thermodynamic status of water, and it is based on temperature-sensitive reactions (see supplementary material S4 for more details about this method). However, also the *P* affects the reaction and, therefore, for a fixed *T*, the percentage of Fe^{3+} content and the pressure value can be simultaneously estimated (see Lanari, 2012; Scheffer et al., 2016; Lanari et al., 2019; Di Rosa et al., 2020; Sanità et al., 2022b). The Wm composition depends on the relative proportions of the end-members Cel, Ms and Prl, which are mostly controlled by the Tschermak and Pyrophyllite substitutions (see Guidotti and Sassi, 1998 for a review).

By combining the *T* and *P* ranges obtained from the Chl-Qz-H_2O and the Phg-Qz-H_2O methods respectively, the *P–T* estimates were calculated with Chl-Phg-Qz-H_2O multiequilibrium thermobarometry (Vidal and Parra, 2000, see supplementary material S4 for more details). Only the Chl-Wm couples whose *P–T* equilibrium is within the *P* and *T* ranges calculated with the two other methods were considered. For this selected group of *P–T* values, a further equilibrium tolerance was set to consider only the *P–T* values to which the minimum Gibbs free energy (<5000 J in this case) is related. Finally, to verify the robustness of our results, a comparison between the classic geo-thermobarometers available in the literature was performed (*i.e.,* Massonne and Schreyer, 1987; Bourdelle and Cathelineau, 2013; Lanari et al., 2014a). According to Vidal and Parra (2000), the absolute uncertainty on *T* and *P* estimates are of ±30 °C and ±0.2 GPa, respectively.

3.2.4 White mica "crystallinity" index and b_0 cell parameters

https://doi.org/10.1180/mgm.2024.80 Published online by Cambridge University Press

X-ray diffraction was used to perform the WmIC and b_0 cell parameter (see supplementary material S5 for more details about the sample preparation). The WmIC was measured on the <2 μm grain-size glycolated powder fraction that was placed on glass slides following the procedure described by Lezzerini et al. (1995). The WmIC measures the changes in the shape (Full Width at Half Maximum, FWHM) of the first basal reflection of Wm grains by X-ray diffraction, which is considered sensitive to temperature variation (Weaver, 1961; Kübler, 1967a, b, 1968; Sassi and Scolari, 1974; Kisch, 1980a, b). The FWHM values expressed in Δ°2θ CuKα units of the Wm 10 Å peaks were reported in the crystallinity index scale (CIS, Warr and Ferreiro Mählmann, 2015). The spectra of each investigated sample are reported in the Figure F3 in the supplementary material S5.

The b_0 parameter was calculated (Sassi and Scolari, 1975; Franceschelli et al., 1989; Guidotti and Sassi, 1989) by measuring the d_{060} spacing in white mica grains using the (211) quartz reflection as an internal standard (*i.e.*, Kisch *et al.*, 2006). The positions of Wm and quartz reflections were defined on randomly oriented whole-rock powders for each metapelite sample. To verify the reliability of the measurement of b_0 values in this work, we performed a further calculation of this parameter using the chemical analyses of Wm, which were observed to be in textural equilibrium with Chl using the equations proposed by Guidotti and Sassi (1989) included in the spreadsheet of Verdecchia et al. (2019). The authors take into account different cation occupancies of Wm, where the condition Na/(Na+K)<0.15 is respected to calculate this parameter: $b_0 = 8.9931 + 0.0440(Mg^{2+} + Fe^{2+} + Fe^{3+})$; $b_0 = 9.1490 - 0.0258(Al^{IV} + Al^{VI})$; and $b_0 = 8.5966 + 0.0666(Si)$. Finally, to verify the robustness of our results for WmIC and b_0, a comparison with the data published in the literature by different authors in the same tectonic unit was performed.

4. Results

4.1 Mineral chemistry

4.1.1 Chlorite

https://doi.org/10.1180/mgm.2024.80 Published online by Cambridge University Press

All the chemical heterogeneity of Chl grains grown along the S1 foliation (D1 chlorites) were considered. Note, that the quality of the chemical compositions of Chl described in this section was evaluated following the recommendations proposed by Vidal and Parra (2000). Although the investigated chlorite is located in the same microdomain (white box of Figures 3e), chemical differences exist (Figures 4a, b). At the microscale (Figure 3e, 4a), detrital Chl along the S0 appears as big stocky crystals with frayed edges and show MgO-rich composition (up to 15 wt. %) than the neo-formed S1 Chl (which tend to have ca 10 wt.% of MgO, yellow line in the Figures 4a). The latter is characterized by crystals with sharp edges never exceeding 20-30 µm in size (Figure 3e). Overall, a core-to-rim decrease of the MgO content can be observed. FeO wt.% tends to be higher in the core of both detrital and syn-metamorphic Chl (Figure 4b). The Al_2O_3 wt% map of Figure 4c shows an enlarged area of the Chl grains that grew along the S1 foliation (white boxes of Figure 4a and b). On it, at least three groups of Chl can be detected (blue, red and green areas in Figure 4c), whose average compositions with the related standard deviations are reported in table 1: the first group is characterized by Al_2O_3 of ca. 23.00 wt.% of; the second group tends to have slightly highest Al_2O_3 content (with a mean value of 23.27 wt.%) while the third group shows a more scattered Al_2O_3 content with a mean value of 21.87 wt.%. XMapTools allow to directly select pixels located in different areas of the X-Ray compositional maps. This tool allowed us to investigate small areas (a few µm-size) of Chl crystals whose chemical analysis cannot be acquired by EPMA. For each group of Chl, the structural formulae were calculated on 14 anhydrous oxygens. The first Chl group is characterized by a XMg mean of 0.42 ± 0.08 (blue dot in Figure 4d); Si contents of 2.75 ± 0.06 atom per formula unit (a.p.f.u., blue dot in Figure 4d, e); Al^{VI} content of 1.63 ± 0.06 a.p.f.u. (Figure 4d). The second group of Chl is characterized by higher XMg with a mean of 0.45 ± 0.05, Si of 2.72 ± 0.04 a.p.f.u, and Al^{VI} similar to the first group chlorites (Figure 4d and e) with 1.60 ± 0.04 a.p.f.u.,. The third group of D1 chlorites is characterized by XMg of 0.34 ± 0.05 and Si mean values of 2.77 ± 0.07 a.p.f.u.and more variable Al^{VI} contents (1.52 ± 0.16 a.p.f.u.) (Figures 4d, e). All D1 chlorite groups have Si contents that never exceed 3.00 a.p.f.u.; the total contents of Mg^{2+} and Fe^{2+} present in the M octahedral site

https://doi.org/10.1180/mgm.2024.80 Published online by Cambridge University Press

(M-site) are greater than 3.50 a.p.f.u. and they show vacancies at values lower than 0.20 a.p.f.u. (Figure 4f). Overall, the D1 chlorite groups show chlinocore (Clc) + daphnite (Dph)-rich compositions (Figure 4f, see also the table 1). The sudoite (Sud) content tend to progressively decrease from the first to the third group of D1 chlorites, while the amesite (Am) content tends to be higher in the second group of chlorites and, generally, never exceeds 30% for all of the chlorites (Figure 4f and Table 1).

4.1.2 White mica

All chemical heterogeneities of the D1 Wm were considered, and the quality of these is based on the recommendations proposed by Vidal and Parra (2000). As for Chl, also detrital Wm appears like big crystals (up to 100 µm in size) characterized by frayed edges, while, the neo-formed ones never exceeding 20-25 µm (Figures 3e, 5). The SiO_2 content ranges between 45 and 55 wt. % (Figure 5a) while the Al_2O_3 tends to be higher (up to 40 wt.%) in the detrital Wm than the neo-formed one (20-35 wt.%, Figure 5b). However, the Al_2O_3 wt.% variation at grain-scale (Figure 5b) sheds light that differences exist for both detrital and syn-metamorphic Wm crystals with a generally core-to-rim decreasing. The Figure 5c show an enlarged area of the investigated X-ray compositional map (white box of Figure 5a, b) where the Si a.p.f.u. variation of all Wm grains along the S1 foliation is represented. The same XMapTools function used for the Chl grains was applied again. At least three groups of Wm, grow along the S1 foliation, can be observed showing textural equilibrium with those detected for Chl (purple box indicates the location of the Chl crystal outlined in Figure 4c). The representative chemical compositions for each group of Wm are reported in the Table 2 and the structural formulae were calculated on 11 anhydrous oxygens The first group shows Si contents with an average value of 3.31 ± 0.02 a.p.f.u. (Figures 5c, d, e), and variable Al^{VI} content (average value: 1.56 ± 0.1 a.p.f.u., Figure 5f, g). The XMg and K content are more variable (average values: 0.46 ± 0.10 and 0.79 ± 0.30 a.p.f.u., respectively - Figures 5d, e). The second group tends to have lower Si

https://doi.org/10.1180/mgm.2024.80 Published online by Cambridge University Press

contents (average: 3.14 ± 0.08 a.p.f.u.) and higher Al^{VI} contents (1.64 ± 0.09 a.p.f.u. Figures 5d, e, f and g). XMg is variable with an average values of 0.52 ± 0.22, while the K contents tend to be less scattered (mean 0.93 ± 0.03 a.p.f.u). The third group shows the lowest values of Si contents (average: 3.11 ± 0.1 a.p.f.u.) and shows the highest K contens (average: 0.98 ± 0.01 a.p.f.u., Figures 5d, e, f). The Al^{VI} content show an average value of 1.66 ± 0.07 a.p.f.u, while XMg is scattered with an average of 0.48 ± 0.18 (Figure 5d, f and g). All analysed Wm groups can be represented by a muscovite (Ms)-celadonite (Cel) solid solution and tend to have Ms-rich compositions, with celadonite and pyrophyllite contents generally not exceeding 30% (Table 2). A slight amount of trioctahedral (Tri) and pyrophyllite (Prl) components never exceed the 25% can be observed (see table 2) in the selected Wm grains. According to Bousquet et al. (2002) the trioctahedral component could be due to the Fe^{3+} content of the Wm.

4.2 Forward thermodynamic modelling

The phase diagrams were computed on a *P–T* space by setting pressure and temperature range of 0.2-1.1 GPa and 200-600 °C. The chemical system used were KFMASH and KFMASHO and Ca, Mn, Ti and Na were removed from the input bulk composition (see the table T4 in the supplementary material S3) because of their minor contents in the observed mineral assemblage found to be in textural equilibrium within the micro-domain of interest (white box of Figure 3e). The model was computed considering FeOtot=Fe^{2+} (Figure 6a), as (Fe-rich) oxides in the investigated domains are scarce or lacking at all. However, a model where FeOtot=Fe^{2+} + Fe^{3+} is performed (a 10% of FeO_{TOT} as Fe^{3+} as suggested by Forshaw and Pattison, 2021, see table T4 in S3) to check if the predicted mineral compositions is still comparable with the observed values (Figure 6b). The lack of carpholite, chloritoid and biotite in the observed mineral assemblage constrains a *P/T* field (marked in red in Figures 6a and b) corresponding to *P* range of 1.1-0.2 GPa and *T* range of 200-550 °C (Figure 6a) and to 1.0-0.2 GPa and 200-375 °C when Fe^{3+} is considered in the input bulk composition (Figure

https://doi.org/10.1180/mgm.2024.80 Published online by Cambridge University Press

6b), in which the predicted mineral assemblage Chl, Wm and Qz matches the observed one. When Fe^{3+} is considered (Figure 6b), the field where the observed mineral assemblage is predicted to be stable is smaller and Hematite (Hem) is modelled (ca. 1%, see table T4 in S3). As the phase proportion of Fe-oxides in the investigated domains is lacking, and also the modal proportion predicted by the model is low (ca. 1%), their occurrence in the *P–T* fields of interest can be neglected. This test suggests that the observed mineral assemblage, phase proportion and compositions, can be predicted keeping $FeO_{TOT} = Fe^{2+}$ or $FeO_{TOT} = Fe^{2+} + Fe^{3+}$ (with a 10% of FeOtot as Fe^{3+}). Besides, the amount of Fe^{3+} used in this work, given the absence of detailed information regarding mineral oxides, could be considered as the maximum value to be used for the observed mineral assemblage to be predicted (according to the suggestions proposed by Forshaw and Pattison, 2021). Ms-rich and Clc+Daph-rich compositions for Wm and Chl are predicted by both models. As the *P–T* field of the investigated mineral assemblage are large (Figure 6a and 6b) we computed also the isopleths contoured for Si content and XMg content of Wm and Chl, respectively (Figure 6c, 6d).

All computed isopleths (for Wm and Chl) intersect within the stability field of the investigated mineral assemblage. The steep trend of XMg contour for Chl allow to us to use it as good *T*-sensitive parameter. For Wm, the Si isopleth shows a *P*- and *T*-dependent trend (Figure 6b). In the model where no Fe^{3+} is considered, the predicted Si content and XMg value (for Wm and Chl, respectively) range from 3.26 and 3.36 and 0.28-0.44, respectively. Similarly, when Fe3+ in considered in the input bulk composition, Si content and XMg values (for Wm and Ch, respectively) are 3.26-3-34 and 0.41-0.44. Note that only the observed Si contents and XMg values of Wm (3.31 ± 0.02 a.p.f.u.) and Chl (0.42 ± 0.08) of the first groups (see the previous section) are coherently predicted by the models. By contrast, the Si and XMg measured for the second and the third groups of Wm and Chl are not predicted by the models. Therefore, taking in mind the observed average values of Si content (for first group Wm) and XMg (for first group Chl) which can be regarded as the maximum values, it is possible to make a comparison with the modelled isopleths. In this approach, we consider intersection between the modelled isopleths is regarded as reliable to estimates of *P* and *T*. When $FeO=Fe^{2+}$ is

https://doi.org/10.1180/mgm.2024.80 Published online by Cambridge University Press

considered, it is not possible to discriminate an area in the *P–T* space because of the missing of clear cross-cutting relationships of the modelled isopleths corresponding to the observed average values of XMg and Si content (Figure 6c). By contrast, in the model where Fe3+ is considered, a good cross-cutting relationship between Si and XMg isopleths of Wm and Chl, respectively, reflect well the observed one and provide *P* and *T* estimates of 275-280 °C and 0.85-0.80 GPa (Figure 6d).

4.3 Inverse modelling for P–T estimates

The results obtained with the Chl-Qz-H_2O (Vidal et al., 2005) and Phg-Qz-H_2O methods allowed us to estimate the *P–T* conditions using local composition of each Chl and Wm groups which were found to be in textural equilibrium along the S1 foliation (see the previous section). The Chl-Qz-H_2O method that was applied on the three groups of Chl present in the microdomain of Figure 4c indicates three different range of chlorite temperature formation (Figure 7a). The results are reported in the distribution histograms (Figure 7a) where along the X-axis the *T* is reported while the height of each bar (Y-axis) represents the number of chlorites formed to a specific temperature range. For each computation related to each Chl group, at least 10% of Fe^{3+} was estimated (by means of ChlMicaEqui minimization function) at fixed pressure value (0.7, 0.5 and 0.4 GPa for the first, the second and the third group of Chl, respectively, see the S4 for details). Each Chl group shows different temperature ranges (Figure 7a) corresponding to the peaks of 170-240 °C, 250-285 °C and 300-335 °C, outlining the occurrence of the three Chl groups along the S1 foliation.

The *P* conditions were estimated using the Phg-Qz-H_2O method (Dubacq et al., 2010) considering only the Wm analyses contained in the *T* range previously defined with Chl-Qz-H_2O. The *P* range for the Wm grains grown along the S1 foliation is thus calculated at a fixed *T* (275, 250 and 320 °C, respectively referred to the average *T* values estimated for different Chl groups) and Fe^{3+} (10-20% of FeO_{TOT}). The results are represented by a line along which the interlayer water content (in the A-site)

https://doi.org/10.1180/mgm.2024.80 Published online by Cambridge University Press

varies by increasing or decreasing *P* and *T*. Three main *P* ranges can be observed, *i.e.*, 0.38-0.21 GPa, 0.61-0.42 GPa and 0.87-0.62 GPa (Figure 7b), supporting that different Wm groups occur along the S1 foliation according with the described mineral chemistry.

The *P–T* estimates obtained with the Chl-Phg-Qz-H_2O multiequilibrium approach (Vidal and Parra, 2000) were compared with the *P* and *T* ranges constrained with the Chl-Qz-H_2O and Phg-Qz-H_2O methods (Figure 7c). The comparison sheds light on the good fit between the three different methods that mark the occurrence of three different clusters of Chl-Wm couples along the S1 foliation (Figure 7c): i) the first cluster is related to the peak pressure conditions (*HP–LT*, 0.85-0.68 GPa and 250-285 °C – Figure 7c, d); the second is related to the peak temperature conditions (low pressure–high temperature - *LP–HT*, 0.6-0.4 GPa and 300-335 °C - Figure 7c, d), while the third cluster is related to the Chl-Wm couple, which is stable at the lowest *P* and *T* conditions (low pressure–low temperature - *LP–LT*, 0.35-0.2 GPa and 235-250 °C – Figure 7c, d).

The obtained results were compared with the pressures and temperatures estimated via classic geothermobarometers (Figure 7c, e and f). We used the calibrations proposed for low-temperature conditions by Lanari et al. (2014), which can be used even if the amount of Fe^{3+} in chlorite is unknown, and by Bourdelle and Cathelineau (2015). The latter calibration was proposed by the authors as an efficient tool to estimate the temperature of chlorite formation (although the nonideal contribution of site mixing is not considered) by means a graphical representation in which Fe^{2+} + Mg^{2+} (M-site) occupancy vs Si content is reported. The first geothermometer (Figure 7e) for the different groups of chlorite grains indicates the following *T* ranges: 250-270 °C for the first group (*HP–LT* chlorites); 310-320 °C for the second group (*LP–HT* chlorites); and 180-240 °C for the third group (*LP–LT* chlorites). The Bourdelle and Cathelineau (2015) geothermometer (Figure 7f) yields three different *T* ranges: the first range is 225-275 °C; the second is 275-325/>325 °C; and the third again 225-275 °C. Altogether, these comparisons show a good fit with the three temperature ranges of chlorite formations modelled with multiequilibrium thermobarometry. The geobarometer of Massonne and Schreyer (1987) (Figure 7c) was used to test our *P* estimates. This geobarometer is

https://doi.org/10.1180/mgm.2024.80 Published online by Cambridge University Press

based on a calibration where the (Fe, Mg) celadonite component of Wm, which is in equilibrium with K-Fsp + Qz + Phlogopite (Phl), is a function of pressure. The pressure range calculated on the Wm grains (values >200 pixel/map) grown along the S1 foliation (histogram reported along the Y-axis of Figure 7c) is 1.2-0.2 GPa, with a peak at 0.5-0.2 GPa.

4.4 WmIC and b_0

The WmIC values with the relative standard deviation, measured along the investigated transect, are shown in the histogram of Figure 8a. The red dashed lines indicate the lower and upper limits of very low-grade metamorphic conditions proposed by Warr and Ferreiro Mählmann (2015). Overall, specimens show fewer variable WmIC distributions ranging from 0.13 to 0.22 Δ°2θ (Figure 8a and table T5 in the supplementary material S5). Mixed layers are not identified (see Figure F2 in supplementary material S5). These data strongly indicate that the Cabanaira Unit reached typical epizone *T* conditions (more than 300 °C) during its deformation history. Overall, the distribution of the WmIC values into the Cabanaira Unit is in good agreement with the microstructural observations and the observed paragenesis.

The b_0 value distribution is represented in the histograms of Figure 8b, with the barometric limit values (blue dashed lines) suggested by Franceschelli et al. (1989). Samples again show less variability in the distribution values of the b_0 cell parameter, with values ranging between 9.006 and 9.018 Å and a peak at 9.011-9.013 Å (Figure 8b). The b_0 values measured on the Cabanaira Unit are within the field related to high-pressure metamorphic field (0.5-0.2 GPa based on Franceschelli et al., 1989). The calculation of the b_0 parameter obtained by taking into account the average chemical compositions of white mica groups (according with Verdecchia et al., 2019) found to be in equilibrium with chlorite grains along the S1 foliation was performed (Figure 8c, see table T6 in

https://doi.org/10.1180/mgm.2024.80 Published online by Cambridge University Press

supplementary materials S5). In the *P/T* space of Figure 8c, the b_0 isopleths (after Guidotti and Sassi, 1986) are indicated. Along the X-axes, the equivalent *T* range related to the measured WmIC index values of powders < 2 μm, is reported. Each point in the *P/T* space represents the b_0 calculated for Wm average compositions related to each group at a *T* corresponding to that estimated for chlorite formation with the Chl-Qz-H_2O thermometer of Vidal et al. (2005). Overall, the *P* ranges obtained from the calculated b_0 values fall within the range estimated with the extrapolated with X-ray powder diffraction. However, these *P* range associated with the b_0 values tend to be related to lower pressure values than those calculated by the barometer of Dubacq et al. (2010) with the *HP–LT* Wm group showing the highest discrepancy.

5. Discussion

5.1 P–T path of the Cabanaira Unit reconstructed by an integrated approach

The integrated approach shown in this work allowed us to reconstruct, for the first time, the *P–T* path for the low-grade Cabanaira Unit (Figure 9) exposed along the southwestern sector of the Marguareis Massif. Microstructural analyses clearly indicate that mineral the assemblage Chl-Wm-Qz are in textural equilibrium, along the S1 foliation micro-site of interest, with no evidence of minerals like carpholite or chloritoid. The thermobarometric estimates show that the prograde path is not recorded by the unit and that the described mineral assemblages are related to the retrograde path only (Figure 9). In the following the different approaches will be discussed taking into account their ability to capture the metamorphic history of the low-grade rocks of interest.

Forward thermodynamic modelling suggests that the observed mineral assemblage is predicted to be stable under a huge range of *P–T* conditions. However, using the isopleths approach and considering the effect of the ferric iron, the *P–T* estimates for the first group of Wm and Chl was constrained (275-280 °C and 0.85-0.80 GPa). However, the occurrence of Wm-Chl groups showing slight

https://doi.org/10.1180/mgm.2024.80 Published online by Cambridge University Press

differences in their chemical compositions and the limited ability to physically select them in order to obtain at least three local bulk compositions make the usage of forward thermodynamic modelling restricted. Notwithstanding, the database used to perform forward thermodynamic modelling yielded realistic results. In fact, the adopted solution models for Wm include pyrophyllite and paragonite as end-members of white-mica solid solution. The stability of paragonite is not expected since the very low Na-content of Wm, even if it cannot be correctly evaluated since Na is not included in the input bulk composition. The possible formation of pyrophyllite predicted by modelling results from a miscibility gap with dioctahedral mica (see Parra et al., 2002), which is not observed in the simulation performed in this work. For the Chl, among the available solid-solution models, those adopted ones in this work (Vidal et al., 2005 with the revised Margules parameters from Vidal et al., 2006) are demonstrated yield more realistic pressure conditions for carpholite-producing reactions (see solution models of Hunziker et al., 2003 where carpholite is predicted to be stable at low *P* conditions). It must be underlined that the chlorite model of Vidal et al. (2005), where Si>3 a.p.f.u. is not allowed and a Sud end-member is included, is not fully compatible with the Theriak-Domino algorithm in which Mg-Fe partitioning cannot be forced. However, the usage of the database of Pourteau et al. (2014) with the solution models chosen in this work (S3 supplementary material) during forward modelling allowed us to compute realistic phase equilibria diagrams even if the observed mineral assemblage is predicted to be stable into a field characterized by a huge range of *P*–*T* conditions.

The reconstructed *P*–*T* path of the Cabanaira Unit reported in Figure 9 was mostly constrained with the use of the multiequilibrium thermobarometry. Inverse thermodynamic modelling applied to the three groups of Wm-Chl couples indicates that different peak *P* and *T* conditions were achieved along the tectono-thermal evolution of the Cabanaira Unit (Figure 9). The peak *P* at 0.85-0.68 GPa and 250-285 °C (which is coherent with the *P*–*T* conditions predicted by forward modelling) were followed by decompressional warming (peak *T*) constrained by the Chl-Wm couples in chemical equilibrium at lower *P* (0.6-0.4 GPa) and higher *T* (300-335 °C) conditions. Note that decompressional warming was also documented in other sectors of the Ligurian Alps (see Maino et al., 2012). The last part of

https://doi.org/10.1180/mgm.2024.80 Published online by Cambridge University Press

the *P–T* path is constrained by the Chl-Wm couples in equilibrium at the lowest *P* and *T* conditions (0.35-0.2 GPa and 235-250 °C). The *P* and *T* estimates for the different groups of Chl-Wm couples show a good fit with the classic geothermobarometers that are usually used for low-grade metamorphism, with the exception of the Massonne and Schreyer (1987) barometer. The latter, in fact, gives pressure values (0.5-0.6 GPa) lower than the peak *P* estimated with multiequilibrium thermobarometry approach. According to Guidotti and Sassi (1998), this is due to the effect of the deviation of the investigated mineral assemblage from the limiting mineral assemblage (*i.e.*, Ms + K-Fsp + Qz + Phl) calibrated by Massonne and Schreyer (1987). In fact, these authors underline that any deviation from the assemblage used to perform their calibration can, at best, give a minimum pressure value.

The WmIC index and the b_0 cell parameter calculated and measured in this work are roughly related to *P* and *T* range which partially fit with the thermobarometric estimates. The measured IC value distribution roughly indicates temperatures 300 °C < *T* < 350 °C, according to Kisch (1987), Niedermayr et al. (1984) and Weaver and Boekstra (1984), which are coherent with the maximum *T* values (peak *T*) estimated with thermobarometry. The measured b_0 value distribution indicates a *P* range related to 0.4-0.6 GPa for the Wm grains (Guidotti and Sassi, 1989; Guidotti et al., 1989; Franceschelli et al., 1989). The calculated b_0 parameters for the Wm crystals used for thermobarometric calculations further provide constraints. The most coherent data are those related to the *LP–HT* Wm, indicating a range of 0.48-0.2 GPa, showing a good fit with the measured b_0 values. Note that the *P* range estimated with the b_0 value tends to be slightly lower than that obtained with the Phg-Qz-H_2O barometer (Dubacq et al., 2010), even if they are within the uncertainty associated with the thermobarometric methods. The b_0 values calculated for the *LP–LT* Wm crystals also indicate *P* conditions comparable to those estimated with thermobarometry (range of 0.32-0.18 GPa, cf. Figure 7c and Figure 8c). The *P* range, extrapolated through the b_0 parameter, calculated for the *HP-LT* Wm chemical analysis shows significant differences compared with those estimated with thermobaric calculation (cf. Figures 7c and 8c). This can be explained considering the remarks

https://doi.org/10.1180/mgm.2024.80 Published online by Cambridge University Press

underlined by Guidotti and Sassi (1976) and Sassi and Scolari (1974), which suggest that the b_0 value measurement (or calculation) shows only a qualitative relation with *P* and it is tested only for a range never exceeding 0.6 GPa. The results beyond this value are therefore not reliable. However, crystallochemical indexes measurement (according to Guidotti and Sassi, 1998; Kubler and Goy-Eggenberger, 2001; Abad and Nieto, 2007; Warr and Ferreiro Mahalman, 2015) show two limits: 1) they do not provide a quantitative estimate of *P* and *T* conditions; and 2) they classically were measured on rock powders where the microtexture is clearly not preserved. These two factors clearly represent the weakness of this method, and mistakes can be made in constraining the metamorphic history of low-grade rocks if the results obtained with these approaches are not verified and/or supported by other methods.

The ranges of *T* estimates get using different approaches, overall indicating no more than 350 °C, are coherent with the observed microstructures resulted from dissolution and re-crystallization processes which were the main deformation mechanisms during the metamorphic history. Similar *T* estimations for the deformed phyllosilicates-rich rocks were yielded by other authors (Buatier et al., 2012; Lacroix et al., 2011; Lacroix and Venneman, 2015; Elmola et al., 2017).

5.2 Assessment of the P–T estimates within the tectonic framework of the Cabanaira Unit

Our data indicate that the Cabanaira Unit recorded a pressure–temperature evolution where peak *P* conditions are followed by decompressional warming (peak *T*). The consistency between this estimate and the tectonic framework proposed for the Cabanaira Unit can be assessed. The first contribution was made by Brizio et al. (1983), in which the authors proposed that the thrusting of the San Remo-Monte Saccarello Unit (cf. Helminthoid Flysch Unit of this work) onto the Briançonnais Units (here represented by the Marguareis Unit, including the Cima del Becco Slices and the Cabanaira Unit) has been responsible for their deformation and the very low-grade metamorphic imprint. In this framework, the peak *P* conditions estimated in this work for the Cabanaira Unit should be due to the

https://doi.org/10.1180/mgm.2024.80 Published online by Cambridge University Press

effect of the lithostatic loading produced by the thrusting of the San Remo-Monte Saccarello Unit (cf. Helminthoid Flysch Unit, this work). However, the estimated thickness of the Helminthoid Flysch Unit succession exposed in the investigated area is not sufficient to produce lithostatic loading to explain the pressure values estimated in this work for the Cabanaira Unit.

Alternatively, Piana et al. (2014) and d'Atri et al. (2016) proposed that this unit shows an Anchizone metamorphic imprint, with temperatures never exceeding 240 °C during its tectonic evolution, and that it developed at very shallow structural levels. This tectonic scenario must now be reconsidered with regard to the *P* and *T* conditions constrained in this work, where temperatures greater than 300 °C and pressures up to 0.8 GPa are well established.

Recently, Sanità et al. (2020) and Sanità (2023) proposed a tectonic evolution in which the thrusting of the Helminthoid Flysch Unit (cf. San Remo-Monte Saccarello Unit, see *syn-stacking tectonics* of Sanità et al., 2020) developed immediately after the D1 phase recorded by the Cabanaira Unit that is thought to have developed during its involvement into the Alpine wedge (see *pre-stacking structures* of Sanità et al., 2020). The reconstructed *P–T* pathway (Figure 9) seems to be coherent with the tectonic setting of Sanità et al. (2020, 2021), where the tectonic evolution of the Cabanaira Unit is thought to have developed during its underthrusting, accretion and subsequent exhumation into the Alpine wedge during the middle to late Eocene. The *P–T* paths of Figure 9 are related to each tectonic unit exposed at the boundary between the Maritime and Ligurian Alps. In this *P*/*T* space, the trajectories followed by each tectonic unit have been reconstructed using multiequilibrium thermobarometry (see Sanità et al., 2022b and 2022c for more details) making the comparison with the estimates performed in this paper justified and reliable. Note that the metamorphic peak *P* conditions of all the units lie along a geothermal gradient coherent with that estimated by different authors for the Western Alps for oceanic (*i.e.*, the Moglio-Testico Unit) and continental (*i.e.*, Margaureis Unit and Cabanaira Unit) subduction settings (Agard et al., 2001; Bousquet et al., 2008; Sterzynsky et al., 2012; Agard et al., 2018; Agard, 2021; Herviou et al., 2022). Interestingly, the peak *P* conditions recorded by the Cabanaira Unit overlap the *P–T* conditions estimated for the exhumation

https://doi.org/10.1180/mgm.2024.80 Published online by Cambridge University Press

of the Marguareis Unit (see D2 phase of Sanità et al., 2022b). However, only the Cabanaira Unit shows warming during decompression with the associated peak *T* conditions close to the classic geothermal gradient typical of the continental collision (30 °C/km) estimated by previous authors for the Alpine belt.

5.3 Factors triggering warming during the exhumation of the Cabanaira Unit

The warming event is well constrained both by multiequilibrium thermobarometry and crystallochemical indexes measurement and it needed to be clarified. There are more factors that could trigger warming, and, in this section, they are taken into account. We explore all the possible processes in which warming can be developed, and they are separately addressed below.

1) Thrusting-related warming. The peak *T* conditions estimated in this work with different methods are strongly in contrast with those calculated by Piana et al. (2014) (Figure 9). These authors, through the WmIC measurement performed on the Roja Unit (cf. Cabanaira Unit of this work) estimated Anchizone field-related temperature conditions never exceeding 200-240 °C by means of the WmIC parameter. Considering that the same methodology and procedure for the IC measurement (see Piana et al., 2014 for more details) have been used, the differences between their data and the results obtained in this work could be due to the location of the sampling. In this work, sampling was performed along a transect on which structural features, such as unit-bounding thrust systems (Figure 2a), occur. The lower crystallinity values (=higher metamorphic temperature conditions, this work), which are supported by the thermobarometric estimates, could be related to the thrust activity largely described in the whole investigated area (Mueller et al., 2020; Sanità et al., 2020; 2021). In contrast, the higher WmIC values (=lower metamorphic temperature conditions) estimated by Piana et al. (2014) were obtained on samples collected in areas where tectonic structures, such as thrusts or fault systems, are lacking. Therefore, having witnessed the impact of this method, the metamorphic temperature conditions calculated in this work could be due to the effect of the thrust activity that was largely documented by several authors in different tectonic settings (*i.e.,* Fernandez-Caliani and

https://doi.org/10.1180/mgm.2024.80 Published online by Cambridge University Press

Galan, 1992; Ducci et al., 1995; Giorgetti et al., 2000; Brogi, 2006; Elmola et al., 2017). In this framework, the peak *T* calculated in this work in the investigated transect could thus be the witness of the syn-coupling tectonic events (cf. *syn-stacking* events of Sanità et al., 2020) largely documented in the mapped area. In this framework, the warming could thus be regarded as related to the thrusting of the Helminthoid Flysch Unit onto the already exhumed Briançonnais Units (*i.e.,* the Cabanaira Unit). Maino et al. (2012), (2015) and (2020) performed an investigation about the thrust activity-related thermal budget on the units exposed above and below the Penninic Front in the Monte Fronté zone. They conclude that the *HT* event is recorded by the rock volumes because of frictional heating due to thrust activity during nappe emplacement processes. Notwithstanding, the temperature proposed by Maino et al. (2020) are not coherent with those estimated in this study being about 80-90 °C lower than our *T*-peak estimates (Tmax= 245 °C vs. 300-335 °C). However, comparable *T* estimations (more than 300 °C) were documented by Balansa et al. (2022) for the Briançonnais Units exposed in the Embrunais-Ubaye sector (Western Alps, Figure 1) and tectonically located under the Parpaillon Unit (cf. Helminthoid Flysch Unit, this work). The authors proposed that the estimated *T* conditions are due to the thrusting of the Parpaillon Unit onto the underlying Briançonnais Units. According to the authors, this hypothesis implies a volume for the Helminthoid Flysch Unit higher than the one shown currently. In fact, in their palinspastic reconstruction, Balansa et al. (2022) proposed that the leading edge of the Parpaillon Unit was located to the west of its current position. Therefore, in the investigated area, the estimated volume of the Helminthoid Flysch Unit probably does not correspond to that during the thrusting event. Therefore, a similar tectonic framework can be taken into account to explain the warming recorded by the Cabanaira Unit in the investigated area. However, this scenario is in contrast with the field constraints available for the tectonic evolution of the investigated area. In fact, according to Sanità et al. (2020), the thrusting of the Helminthoid Flysch Unit postdates the folding system affecting the Cabanaira Unit (D1 phase), during which warming has been recorded.

https://doi.org/10.1180/mgm.2024.80 Published online by Cambridge University Press

2) Fluid–rock interactions. Fluid–rock interaction cannot a priori be excluded. Hydrothermal circulation was documented in analogue units exposed along the outer sectors of the southwestern Alps by previous authors (cf. Entracque Unit of Barale et al., 2016; Bertok et al., 2019). The authors invoke the occurrence of fault systems that were used as preferred channels for hot fluid circulation. These are interpreted as responsible for the chemical transformation of the host rock and for the variation in the mineral chemistry before the deformation starts to be recorded by the unit. Moreover, fluid circulation into the subduction zone at shallower structural levels cannot be excluded. In fact, dehydration pulses within the subduction zone were outlined as key features contributing to rapid warming during the onset of exhumation (Camacho et al., 2005; John et al., 2012; Dragovic et al., 2015), even if their role is still far from being understood. Notwithstanding, these hypotheses are in contrast with the dataset collection shown in this work because i) the *T* estimated (at least 350 °C) for the hot fluids (Barale et al., 2016; Bertok et al., 2019) is higher than our temperature estimates (peak *T*: 300-335 °C); ii) in the study area, field evidence of an extended early faulting event was not documented, and the peak *T* is constrained to the deformation of the Cabanaira Unit (*i.e.,* during its exhumation towards the surface, D1 phase). Moreover, the role of fluids to the thermal budget during faulting was also investigated by Maino et al. (2020). However, the authors conclude that fluid-rock interaction effect to the thermal budget is neglectable.

3) Perturbation of the geothermal gradient. The warming could be due to a progressive variation in the Alpine wedge thermal state as a result of the beginning of the continental collision, which was documented in other sectors of the belt where its effects are more pronounced (*i.e.*, Goffé et al., 2004; Bousquet et al., 2008; Handy et al., 2010) and in Alpine Corsica (*i.e.*, Di Rosa et al., 2019; Di Rosa et al., 2020 and quoted references). Many contributions have stressed the factors influencing the thermal structure of orogenic belts, such as shear and/or radioactive heating, as well as the thermal conditions of subducting and overriding plates (Gerya et al., 2008; Syracuse et al., 2010; Facenna et al., 2014; Zheng et al., 2016; Regorda et al., 2021). Anomalously, high-temperature events are thought to have developed during incipient continental collision (Gerya et al., 2008), even if

https://doi.org/10.1180/mgm.2024.80 Published online by Cambridge University Press

associated with partial melting (Burg and Gerya, 2005). Amadori et al. (2023) proposed a geological scenario in which the mantle upwelling is invoked to account the hot and shallow thermal signal recorded by the sediments in the late Eocene-late Miocene epi-sutural basin (*i.e.*, the Tertiary Piedmont Basin).

Unfortunately, the current knowledge based on the data shown in this work or available from previously published works is not able to provide a clear snapshot, and therefore, the hypotheses discussed in this paper need further investigation to be supported.

6. Conclusions

This work outlines the paramount importance of a multidisciplinary approach to perform geological surveys aimed to investigate orogenic mechanisms recorded by very low- to low-grade units exposed in the outer sectors of collisional belts. Quantitative and qualitative methods were tested together for reconstruction of the *P–T* path of low-grade meta-pelites, capturing as many segments of it as possible. Each method allowed us to constrain a different part of the metamorphic history of the Cabanaira Unit. The good agreement between estimates from inverse (multiequilibrium thermobarometry) and forward modelling (pseudosection) and crystallochemical indexes measurement, taking into consideration the strengths and weaknesses of each method, allows us to regard them as suitable to reconstruct the *P–T* path of low-grade rocks. Multiequilibrium thermobarometry together with high-resolution quantitative compositional mapping remain the best method to unveil the metamorphic history of low-grade rocks in details.

The *P–T* estimates for the Cabanaira Unit indicate peak *P* conditions (0.85-0.68 GPa and 250-285 °C) that are coherent with the geological models that imply its involvement in the subduction zone during its underthrusting and accretion into the Alpine wedge. In addition, the peak *T* (0.4-0.6 GPa and 300-335 °C) conditions (decompressional warming) were achieved during exhumation after the

https://doi.org/10.1180/mgm.2024.80 Published online by Cambridge University Press

peak *P*. The causes triggering the warming recorded by the Cabanaira Unit are far from being understood, and its tectonic meaning, based on the current knowledge, can only be postulated.

Acknowledgements

The authors thank Tim Johnson and Arne Willner for their very useful and stimulating comments and suggestions, which improved the final version of the manuscript. We also thank the editor for managing the paper. Andrea Risplendente is thanked for his assistance with the EPMA data collection.

Author contribution

Conceptualization: ES; **Methodology**: ES, MDR; **Software**: ES, MDR; **Validation**: ES, MDR, JML, ML, MT, MM, LP; **Formal analysis**: ES; **Investigation**: ES; **Resources**: ES; **Data Curation**: ES. MDR; **Writing original draft**: ES; **Writing - Review & Editing**: ES, MDR, JML, ML, MT, MM, LP**; Visualization**: ES; **Supervision**: JML, MM, LP; **Project administration**: ES, LP.

Data availability statement

Data available from the authors on request.

https://doi.org/10.1180/mgm.2024.80 Published online by Cambridge University Press

Funding statement

This study was funded by PRIN project 2020 (PI Michele Marroni).

Conflict of interest disclosure

The authors declare no conflict of interest.

References

Abad I. and Nieto F. (2007) Physical meaning and applications of the illite Kübler index: measuring reaction progress in low-grade metamorphism. Diagenesis and Low-Temperature Metamorphism, Theory, Methods and Regional Aspects, Seminarios. Sociedad Espanola: Sociedad Espanola Mineralogia, 53-64.

Agard P., Vidal O. and Goffé B. (2001) Interlayer and Si content of phengite in HP–LT carpholite-bearing metapelites. *Journal of Metamorphic Geology*, **19**, 479-495.

Agard P., Plunder A., Angiboust S., Bonnet G. and Ruh J. (2018) The subduction plate interface: Rock record and mechanical coupling (from long to short timescales). *Lithos*, **320**, 537-566.

Airaghi L., Lanari P., de Sigoyer J. and Guillot S. (2017) Microstructural vs compositional preservation and pseudomorphic replacement of muscovite in deformed metapelites from the Longmen Shan (Sichuan, China). *Lithos*, **282**, 262-280.

https://doi.org/10.1180/mgm.2024.80 Published online by Cambridge University Press

Amadori C., Maino M., Marini M., Casini L., Carrapa B., Jepson G. and Di Giulio A. (2023) The role of mantle upwelling on the thermal history of the Tertiary-Piedmont Basin at the Alps-Apennines tectonic boundary. *Basin Research*, **35**, 1228-1257.

Balansa J., Lahfid A., Espurt N., Hippolyte J.C., Henry P., Caritg S. and Fasentieux B. (2022) Unraveling the eroded units of mountain belts using RSCM thermometry and cross-section balancing: example of the southwestern French Alps. *International Journal of Earth Sciences*, 1-16.

Barale L., Bertok C., Salih Talabani N., d'Atri A., Martire L., Piana F. and Préat A. (2016) Very hot, very shallow hydrothermal dolomitization: An example from the Maritime Alps (north-west Italy–south-east France). *Sedimentology*, **63**(7), 2037-2065.

Barbero E., Di Rosa M., Pandolfi L., Delavari M., Dolati A., Zaccarini F. and Marroni M. (2023) Deformation history and processes during accretion of seamounts in subduction zones: The example of the Durkan Complex (Makran, SE Iran). *Geoscience Frontiers*, **14**(2), 101522.

Beltrando M., Compagnoni R. and Lombardo B (2010) (Ultra-) High-pressure metamorphism and orogenesis: an Alpine perspective. *Gondwana Research*, **18**(1), 147-166.

Berman R.G. (1988) Internally-consistent thermodynamic data for minerals in the system Na2O-K2O-CaO-MgO-FeO-Fe2O3-Al2O3-SiO2-TiO2-H2O-CO2. *Journal of Petrology*, **29**(2), 445-522.

Bertok C., Musso A., d'Atri A., Martire L. and Piana F. (2018) Geology of the Colle di Tenda–Monte Marguareis area (Ligurian Alps, NW Italy). *Journal of Maps*, **14**(2), 542-551.

https://doi.org/10.1180/mgm.2024.80 Published online by Cambridge University Press

Bersezio R., Barbieri P. and Mozzi R. (2002) Redeposited limestones in the Upper Cretaceous succession of the Helvetic Argentera Massif at the Italy-France border. *Eclogae Geol Helvetie*, **95**, 15-30.

Bonini L., Dallagiovanna G. and Seno S. (2010) The role of pre-existing faults in the structural evolution of thrust systems: Insights from the Ligurian Alps (Italy). *Tectonophysics*, **480**(1-4), 73-87.

Bonnet G., Chopin C., Locatelli M., Kylander-Clark A.R. and Hacker B.R. (2022) Protracted Subduction of the European Hyperextended Margin Revealed by Rutile U-Pb Geochronology Across the Dora-Maira Massif (Western Alps). *Tectonics*, **41**(4), e2021TC007170.

Bourdelle F. and Cathelineau M. (2015) Low-temperature chlorite geothermometry: a graphical representation based on a T–R2+–Si diagram. *European Journal of Mineralogy*, **27**(5), 617-626.

Buatier M.D., Lacroix B., Labaume P., Moutarlier V., Charpentier D., Sizun J.P. and Travé A. (2012) Microtextural investigation (SEM and TEM study) of phyllosilicates in a major thrust fault zone (Monte Perdido, southern Pyrenees): impact on fault reactivation. *Swiss Journal of Geoscience*, **105**, 313-324.

Bousquet R., Goffé B., Vidal O., Oberhänsli R. and Patriat M. (2002) The tectono-metamorphic history of the Valaisan domain from the Western to the Central Alps: New constraints on the evolution of the Alps. *Geological Society American Bulletin*, **114**(2), 207-225.

https://doi.org/10.1180/mgm.2024.80 Published online by Cambridge University Press

Bousquet R., Oberhänsli R., Goffé B., Wiederkehr M., Koller F., Schmid S.M. and Martinotti G. (2008) Metamorphism of metasediments at the scale of an orogen: a key to the Tertiary geodynamic evolution of the Alps. *Geological Society of London, Special Publications*, **298**(1), 393-411.

Brizio D., Deregibus C., Eusebio A., Gallo M., Gosso G. and Rattalino E. (1983) Guida all'escursione: i rapporti tra la zona brianzonese ligure e il Flysch a elmintoidi, Massiccio del Marguaréis (Limone Piemonte-Certosa di Pesio, Cuneo 14/15 settembre 1983). *Memorie della Società Geologica Italiana*, **26**(2), 579-595.

Brogi A. (2006) Evolution, formation mechanism and kinematics of a contractional shallow shear zone within sedimentary rocks of the Northern Apennines (Italy). *Eclogae Geologicae Helvetie*, **99**, 29-47.

Camacho A., Lee J.K., Hensen B.J. and Braun J. (2005) Short-lived orogenic cycles and the eclogitization of cold crust by spasmodic hot fluids. *Nature*, **435**(7046), 1191-1196.

Capponi G. and Crispini L. (2002) Structural and metamorphic signature of alpine tectonics in the Voltri Massif (Ligurian Alps, North-Western Italy). *Eclogae Geologicae Helvetie*, **95**(1), 31-42.

Capponi G. and Crispini L., Federico L., Piazza M. and Fabbri B. (2009) Late Alpine tectonics in the Ligurian Alps: constraints from the Tertiary Piedmont Basin conglomerates. *Geological Journal*, **44**(2), 211-224.

Carminati E. (2001) Incremental strain analysis using two generations of syntectonic coaxial fibres: an example from the Monte Marguareis Briançonnais cover nappe (Ligurian Alps, Italy). *Journal of Structural Geology*, **23**(9), 1441-1456.

https://doi.org/10.1180/mgm.2024.80 Published online by Cambridge University Press

Chiesa S., Cortesogno L., Forcella F., Galli M., Messiga B., Pasquar G., Pedemonte G.M., Piccardo G.B. and Rossi P.M. (1975) Assetto strutturale ed interpretazione geodinamica del Gruppo di Voltri. *Bollettino della Società Geologica Italiana*, **94**, 555-581.

Collet A., Regnault O., Ozhogin A., Imantayeva A. and Garnier L (2022) Three-dimensional reactive transport simulation of Uranium in situ recovery: Large-scale well field applications in Shu Saryssu Bassin, Tortkuduk deposit (Kazakhstan). *Hydrometallurgy*, **211**, 105873.

Connolly J.A. (2005) Computation of phase equilibria by linear programming: a tool for geodynamic modeling and its application to subduction zone decarbonation. *Earth Planetary Science Lettters*, **236**(1-2), 524-541.

d'Atri A., Piana F., Barale L., Bertok C. and Martire L. (2016) Geological setting of the southern termination of Western Alps. *International Journal of Earth Sciences*, **105**, 1831-1858.

De Andrade V., Vidal O., Lewin E., O'brien P. and Agard P. (2006) Quantification of electron microprobe compositional maps of rock thin sections: an optimized method and examples. *Journal of Metamorphic Geology*, **24**(7), 655-668.

Debelmas J., Kerckhove C., Monjuvent G., Mouterde R. and Pêcher A. (1980). Carte géologique de la France (1/50 000), feuille Orcières (846). BRGM, Orléans.

de Capitani C. and Petrakakis K. (2010) The computation of equilibrium assemblage diagrams with Theriak/Domino software. *American Mineralogist*, **95**(7), 1006-1016.

https://doi.org/10.1180/mgm.2024.80 Published online by Cambridge University Press

Decarlis A., Dallagiovanna G., Lualdi A., Maino M. and Seno S. (2013) Stratigraphic evolution in the Ligurian Alps between Variscan heritages and the Alpine Tethys opening: A review. *Earth Science Review*, **125**, 43-68.

Di Giulio A. (1988) Structural evolution of S. Remo and Moglio-Testico units (Piemontese-Ligurain Flysch, Maritime Alps): *Abstract Rendiconti della Società Geologica Italiana*, **11**, 61-64.

Di Giulio A. (1992) The evolution of the Western Ligurian Flysch Units and the role of mud diapirism in ancient accretionary prisms (Maritime Alps, Northwestern Italy). *Geol Rund*, **81**, 655-668.

Di Rosa M., Frassi C., Meneghini F., Marroni M., Pandolfi L. and De Giorgi A. (2019) Tectono-metamorphic evolution of the European continental margin involved in the Alpine subduction: New insights from Alpine Corsica, France. *Comptes Rendue of Geoscience*, **351**(5), 384-394.

Di Rosa M., Frassi C., Malasoma A., Marroni M., Meneghini F. and Pandolfi L. (2020) Syn-exhumation coupling of oceanic and continental units along the western edge of the Alpine Corsica: A review. *Ofioliti*, **45**(2), 71-102.

Dragovic B., Baxter E.F. and Caddick M.J. (2015) Pulsed dehydration and garnet growth during subduction revealed by zoned garnet geochronology and thermodynamic modeling, Sifnos, Greece. *Earth Planetary Science Letters*, **413**, 111-122.

Dubacq B. (2008) *Thermodynamique des phyllosilicates de basse température: de l'approche macroscopique à la simulation atomistique*. Dissertation, Université Joseph-Fourier-Grenoble I.

https://doi.org/10.1180/mgm.2024.80 Published online by Cambridge University Press

Dubacq B., Vidal O. and De Andrade V. (2010) Dehydration of dioctahedral aluminous phyllosilicates: thermodynamic modelling and implications for thermobarometric estimates. *Contribution to Mineralogy and Petrology*, **159**, 159-174.

Ducci M., Leoni L., Marroni M. and Tamponi M. (1995) Determinazione del grado metamorfico delle Argille a Palombini dell'Alta Val Lavagna (UnitaGottero, Appennino Settentrionale. *Atti della Società Toscana di Scienze Naturali, Memorie, Serie A*, 102.

Duesterhoeft E. and Lanari P. (2020) Iterative thermodynamic modelling—Part 1: A theoretical scoring technique and a computer program (Bingo-Antidote). Journal of Metamorphic Geology, **38**(5), 527-551.

Dumont T., Simon-Labric T., Authemayou C. and Heymes T. (2011) Lateral termination of the north-directed Alpine orogeny and onset of westward escape in the Western Alpine arc: Structural and sedimentary evidence from the external zone. *Tectonics*, **30**(5).

Dumont T., Schwartz S., Guillot S., Malusa M., Jouvent M., Monié P. and Verly A. (2022) Cross-propagation of the western Alpine orogen from early to late deformation stages: Evidence from the Internal Zones and implications for restoration. *Earth Science Review*, 104106.

Abd Elmola A., Charpentier D., Buatier M., Lanari P. and Monie P. (2017) Textural-chemical changes and deformation conditions registered by phyllosilicates in a fault zone (Pic de Port Vieux thrust, Pyrenees). *Applied Clay Science*, **144**, 88-103.

https://doi.org/10.1180/mgm.2024.80 Published online by Cambridge University Press

Escher A., Hunziker J.C., Marthaler M., Masson H., Sartori M. and Steck A. (1997) Geological framework and structural evolution of the Western Swiss-Italian Alps. Deep Structure of the Swiss Alps: Results of the National Research Program 20 (NRP 20), 205-222.

Faccenna C., Becker T.W., Auer L., Billi A., Boschi L., Brun J.P. and Serpelloni E. (2014) Mantle dynamics in the Mediterranean. *Review Geophysics*, **52**(3), 283-332.

Fernández-Caliani J.C. and Galán E. (1992) Influence of tectonic factors on illite crystallinity: a case study in the Iberian pyrite belt. *Clay Minerals*, **27**(3), 385-388.

Ford M., Lickorish W.H., Kusznir N.J. (1999) Tertiary foreland sedimentation in the Southern Subalpine Chains, SE France: a geodynamic appraisal. Basin research, **11**(4), 315-336.

Ford M. and Lickorish W.H. (2004) Foreland basin evolution around the western Alpine Arc. *Geological Society of London, Special Publications*, **221**(1), 39-63.

Ford M., Duchêne S., Gasquet D. and Vanderhaeghe O. (2006) Two-phase orogenic convergence in the external and internal SW Alps. *Journal of Geological Society*, **163**, 815-826.

Forshaw J.B., Pattison D.R. (2021) Ferrous/ferric (Fe2+/Fe3+) partitioning among silicates in metapelites. *Contribution to Mineralogy and Petrology*, **176**(9), 63.

Franceschelli M., Battaglia S., Cruciani G., Pasci S. and Puxeddu M. (2017) Very low-temperature metamorphism in Ordovician metasedimentary rocks above and below the Sardic unconformity, SW Sardinia, Italy. *International Journal of Earth Sciences*, **106**, 531-548.

https://doi.org/10.1180/mgm.2024.80 Published online by Cambridge University Press

Frassi C., Di Rosa M., Farina F., Pandolfi L. and Marroni M. (2022) Anatomy of a deformed upper crust fragment from western Alpine Corsica (France): insights into continental subduction processes. *International Geology Review*, 1-21.

Gerya T.V., Perchuk L.L. and Burg J.P. (2008) Transient hot channels: perpetrating and regurgitating ultrahigh-pressure, high-temperature crust–mantle associations in collision belts. *Lithos*, **103**(1-2), 236-256.

Ghignone S., Sudo M., Balestro G., Borghi A., Gattiglio M., Ferrero S. and Van Schijndel V. (2021) Timing of exhumation of meta-ophiolite units in the Western Alps: New tectonic implications from 40Ar/39Ar white mica ages from Piedmont Zone (Susa Valley). *Lithos*, **404**, 106443.

Gidon M. (1972) Les chaînons briançonnais et subbriançonnais de la rive gauche de la Stura entre le Val de l'Arma (province de Cuneo Italie). *Géologie Alpine*, **48**(1), 87-120.

Giorgetti G., Memmi I. and Peacor D.R. (2000) Retarded illite crystallinity caused by stressinduced sub-grain boundaries in illite. *Clay Minerals*, **35**(4), 693-708.

Goffé B., Schwartz S., Lardeaux J.M. and Bousquet R. (2004) Metamorphic structure of the western and Ligurian Alps. In: *Explanatory note to the map "metamorphic structure of the Alps"* R. Oberhansli (Ed.), Mitt, Österr, Mineral, Gesell, pp 125-144.

Gratier J.P., Dysthe D.K. and Renard F., (2013) The role of pressure solution creep in the ductility of the Earth's upper crust. *Advances in Geophysics*, **54**, 47–179.

https://doi.org/10.1180/mgm.2024.80 Published online by Cambridge University Press

Green E.C.R., White R.W., Diener J.F.A., Powell R., Holland T.J.B. and Palin R.M. (2016) Activity–composition relations for the calculation of partial melting equilibria in metabasic rocks. *Journal of Metamorphic Geology*, **34**(9), 845-869.

Groppo C., Ferrando S., Gilio M., Botta S., Nosenzo F., Balestro G. and Rolfo F. (2019) What's in the sandwich? New P–T constraints for the (U) HP nappe stack of southern Dora-Maira Massif (Western Alps). *European Journal of Mineralogy*, **31**(4), 665-683.

Groshong Jr R.H. (1988) Low-temperature deformation mechanisms and their interpretation. *Geological Society of American Bulletin*, **100**(9), 1329-1360.

Guidotti C.V. and Sassi F.P. (1976) Muscovite as a Petrogenetic Indicator Mineral in Pelitic Schists. *Neues. Jb. Miner. Abh*. **127**, 97-142.

Guidotti C.V. and Sassi F.P. (1986) Classification and correlation of metamorphic facies series by means of Miscovite b (0) data from low-grade metapelites. *Neues. Jb. Miner. Abh*, **153**(3), 363-380.

Guidotti C.V., Sassi F.P. and Blencoe J.G. (1989) Compositional controls on the a and b cell dimen sions of muscovite 2Mi. *European Journal of Mineralogy*, **1**, 71-84.

Guidotti C.V. and Sassi F.P. (1998) Petrogenetic significance of Na-K white mica mineralogy: Recent advances for metamorphic rocks. *European Journal of Mineralogy*, 815-854.

https://doi.org/10.1180/mgm.2024.80 Published online by Cambridge University Press

Handy M.R., Schmid S.M., Bousquet R., Kissling E. and Bernoulli D. (2010) Reconciling plate-tectonic reconstructions of Alpine Tethys with the geological–geophysical record of spreading and subduction in the Alps. *Earth Science Review*, **102**(3-4), 121-158.

Herviou C., Agard P., Plunder A., Mendes K., Verlaguet A., Deldicque D. and Cubas N. (2022) Subducted fragments of the Liguro-Piemont ocean, Western Alps: Spatial correlations and offscraping mechanisms during subduction. *Tectonophysics*, **827**, 229267.

Hirth G. and Tullis J.A.N. (1992) Dislocation creep regimes in quartz aggregates. *Journal of Structural Geology*, **14**(2), 145-159.

Holland T.J.B. and Powell R. (2011) An improved and extended internally consistent thermodynamic dataset for phases of petrological interest, involving a new equation of state for solids. *Journal of Metamorphic Geology*, **29**(3), 333-383.

Hunziker P. (2003) *The stability of tri-octaedrial Fe2+–Mg–Al chlorite. A combined experimental and theoretical study*. Dissertation. Universität Basel.

John T., Gussone N., Podladchikov Y.Y., Bebout G.E., Dohmen R., Halama R. and Seitz H.M. (2012) Volcanic arcs fed by rapid pulsed fluid flow through subducting slabs. *Nature Geosciences*, **5**(7), 489-492.

Kisch H.J. (1980a) Incipient metamorphism of Cambro-Silurian clastic rocks from the Jåmtland Supergroup, Central Scandinavian Caledonides, Western Sweden: illite crystallinity and'vitrinite'reflectance. *Journal of Geological Society*, **137**(3), 271-288.

https://doi.org/10.1180/mgm.2024.80 Published online by Cambridge University Press

Kisch H.J. (1980) Illite crystallinity and coal rank associated with lowest-grade metamorphism of the Taveyanne greywacke in the Helvetic zone of the Swiss Alps. *Swiss Journal of Geosciences*, *73*(3), 753-777.

Kisch H.J. (1987) Correlation between indicators of very low-grade metamorphism. In: *Low Temperature Metamorphism* (Frey, M. (ed.), Blackie & Son, Glasgow, pp. 227-300.

Kisch H.J., Sassi R. and Sassi F.P. (2006) The b0 lattice parameter and chemistry of phengites from HP/LT metapelites. *European Journal of Mineralogy*, **18**(2), 207-222.

Kubler B. (1967a) La cristallinité de l'illite et les zones tout a fait superieours du métamorphisme. Colloque sur le "Etages tectoniques", Neuchatel, Festschrift, 105-122.

Kubler B. (1967b) Anchimétamorphisme et schistosite. Bulletin Centre de Recherches de Pau SNPA, 1, 259-278.

Kubler B. and Goy-Eggenberger D. (2001) The crystallinity of illite revisited: a review of knowledge acquired. *Clay Minerals*, **36**, 143-157.

Lacroix B., Buatier M., Labaume P., Trave A., Dubois M. Charpentier D., Ventalon S., Convert-Gaubier D. (2011) Microtectonic and geochemical characterization of thrusting in a foreland basin: example of the South-Pyrenean orogenic wedge (Spain). *Journal of Structural Geology*, **33**, 1359-1377.

https://doi.org/10.1180/mgm.2024.80 Published online by Cambridge University Press

Lacroix B. and Vennemann T. (2015) Empirical calibration of the oxygen isotope fractionation between quartz and Fe–Mg-chlorite. *Geochemica and Cosmochimica Acta*, **149**, 21-31.

Lagabrielle Y., Brovarone A.V. and Ildefonse B. (2015) Fossil oceanic core complexes recognized in the blueschist metaophiolites of Western Alps and Corsica. *Earth Science Review*, **141**, 1-26.

Lanari P. (2012) *Micro-cartgraphie P-T-dans les roches metamorphiques. Applications aux Alpes et à l' Himalaya*. Dissertation. Université de Grenoble.

Lanari P., Guillot S., Schwartz S., Vidal O., Tricart P., Riel N. and Beyssac O. (2012) Diachronous evolution of the alpine continental subduction wedge: evidence from P–T estimates in the Briançonnais Zone houillère (France–Western Alps). *Journal of Geodynamics*, **56**, 39-54.

Lanari P., Rolland Y., Schwartz S., Vidal O., Guillot S., Tricart P. and Dumont T. (2014) P–T–t estimation of deformation in low-grade quartz-feldspar-bearing rocks using thermodynamic modelling and 40Ar/39Ar dating techniques: example of the Plan-de-Phasy shear zone unit (Briançonnais Zone, Western Alps). *Terra Nova*, **26**(2), 130-138.

Lanari P., Vidal O., De Andrade V., Dubacq B., Lewin E., Grosch E.G. and Schwartz S. (2014) XMapTools: A MATLAB©-based program for electron microprobe X-ray image processing and geothermobarometry. *Computers and Geosciences*, **62**, 227-240.

Lanari P. and Engi M. (2017) Local bulk composition effects on metamorphic mineral assemblages. *Review in Mineralogy and Geochemistry*, **83**(1), 55-102.

https://doi.org/10.1180/mgm.2024.80 Published online by Cambridge University Press

Lanari P. and Duesterhoeft E. (2019) Modeling metamorphic rocks using equilibrium thermodynamics and internally consistent databases: Past achievements, problems and perspectives. *Journal of Petrology*, **60**(1), 19-56.

Lanari P., Vho A., Bovay T., Airaghi L. and Centrella S. (2019) Quantitative compositional mapping of mineral phases by electron probe micro-analyser. *Geological Society of London*, London, Special Publications, **478**(1), 39-63.

Lanteaume M. (1968) Contribution à l'étude géologique des Alpes Maritimes franco-italiennes (p. 405). Impr. nationale.

Lardeaux J.M. and Spalla M.I. (1991) From granulites to eclogites in the Sesia zone (Italian Western Alps): a record of the opening and closure of the Piedmont ocean. *Journal of Metamorphic Geology*, **9**(1), 35-59.

Lardeaux J.M., Schwartz S., Tricart P., Paul A., Guillot S., Béthoux N. and Masson F. (2006) A crustal-scale cross-section of the south-western Alps combining geophysical and geological imagery. *Terra Nova*, **18**(6), 412-422.

Lardeaux J.M. (2014) Deciphering orogeny: a metamorphic perspective Examples from European Alpine and Variscan beltsPart II: Variscan metamorphism in the French Massif Central–A review. *Bullletin de la Societe Géologique de France*, **185**(5), 281-310.

Lezzerini M., Sartori F. and Tamponi M. (1995) Effect of amount of material used on sedimentation slides in the control of illite "crystallinity" measurements. *European Journal of Mineralogy*, **7**, 819-823.

https://doi.org/10.1180/mgm.2024.80 Published online by Cambridge University Press

Lotout C., Poujol M., Pitra P., Anczkiewicz R. and Van Den Driessche J. (2020) From burial to exhumation: Emplacement and metamorphism of mafic eclogitic terranes constrained through multimethod petrochronology, case study from the Lévézou Massif (French Massif Central, Variscan Belt). *Journal of Petrology*, **61**(4), egaa046.

Maino M., Dallagiovanna G., Dobson K.J., Gaggero L., Persano C., Seno S. and Stuart F.M. (2012) Testing models of orogen exhumation using zircon (U–Th)/He thermochronology: Insight from the Ligurian Alps, Northern Italy. *Tectonophysics*, **560**, 84-93.

Maino M., Casini L., Ceriani A., Decarlis A., Di Giulio A., Seno S. and Stuart F.M. (2015) Dating shallow thrusts with zircon (U-Th)/He thermochronometry-The shear heating connection. *Geology*, **43**, 495-498.

Maino M. and Seno S. (2016) The thrust zone of the Ligurian Penninic basal contact (Monte Fronté, Ligurian Alps, Italy). *Journal of Maps*, **12**, 341-351.

Maino M., Casini L., Boschi C., Di Giulio A., Setti M. and Seno S. (2020) Time-dependent heat budget of a thrust from geological records and numerical experiments. *Journal of Geophysics Research,* Solid Earth, 125.

Marotta A.M., Roda M., Conte K. and Spalla M.I. (2018) Thermo-mechanical numerical model of the transition from continental rifting to oceanic spreading: the case study of the Alpine Tethys. *Geological Magazine*, **155**(2), 250-279.

https://doi.org/10.1180/mgm.2024.80 Published online by Cambridge University Press

Marmo B.A., Clarke G.L. and Powell R. (2002) Fractionation of bulk rock composition due to porphyroblast growth: effects on eclogite facies mineral equilibria, Pam Peninsula, New Caledonia. *Journal of Metamorphic Geology*, **20**(1), 151-165.

Michard A., Avigad D., Goffé B. and Chopin C. (2004) The high-pressure metamorphic front of the south Western Alps (Ubaye-Maira transect, France, Italy). *Schweiz. Mineral. Petrogr. Mitt*, **84**, 215-235.

Michard A., Schmid S.M., Lahfid A., Ballèvre M., Manzotti P., Chopin C. and Dana D. (2022) The Maira-Sampeyre and Val Grana Allochthons (south Western Alps): review and new data on the tectonometamorphic evolution of the Briançonnais distal margin. *Swiss Journal of Geoscience*, **115**(1), 1-43.

Massone H.J. and Schreyer W. (1987) Phengite geobarometry based on the limiting assemblage with K-feldspar, phlogopite and quartz. *Contribution to Mineralogy and Petrology*, **96**, 212–224

Mueller P., Langone A., Patacci M. and Di Giulio A. (2018) Detrital signatures of impending collision: The deep-water record of the Upper Cretaceous Bordighera Sandstone and its basal complex (Ligurian Alps, Italy). *Sedimentary Geology*, **377**, 147-161.

Mueller P., Langone A., Patacci M. and Di Giulio A (2020) Towards a Southern European Tethyan Palaeomargin provenance signature: sandstone detrital modes and detrital zircon U–Pb age distribution of the Upper Cretaceous–Paleocene Monte Bignone Sandstones (Ligurian Alps, NW Italy). *International Journal of Earth Science*, **109**, 201-220.

https://doi.org/10.1180/mgm.2024.80 Published online by Cambridge University Press

Mueller P., Maino M. and Seno S. (2020) Progressive deformation patterns from an accretionary prism (Helminthoid Flysch, Ligurian Alps, Italy). *Geosciences*, **10**(1), 26.

Muirhead D. K., Bond C. E., Watkins H., Butler R. W. H., Schito A., Crawford Z. and Marpino A. (2020). Raman spectroscopy: an effective thermal marker in low temperature carbonaceous fold–thrust belts. *Geological Society, London, Special Publications*, **490**(1), 135-151.

Parra T., Vidal O. and Agard P. (2002) A thermodynamic model for Fe-Mg dioctahedral K white micas using data from phase-equilibrium experiments and natural pelitic assemblages. *Contribution to Mineralogy and Petrology*, **143**, 706-732.

Passchier C.W. and Trouw R.A. (2005) *Microtectonics*. Springer Science & Business Media.

Perotti E., Bertok C., d'Atri A., Martire L., Piana F. and Catanzariti R. (2012) A tectonically-induced Eocene sedimentary mélange in the West Ligurian Alps, Italy. *Tectonophysics*, **568**, 200-214.

Piana F., Battaglia S., Bertok C., d'Atri A., Ellero A., Leoni L. and Perotti E. (2014) Illite (KI) and chlorite (AI)"crystallinity" indices as a constraint for the evolution of the External Briançonnais Front in Western Ligurian Alps (NW Italy). *Italian Journal of Geosciences*, **133**(3), 445-454.

Piana F., Barale L., Bertok C., d'Atri A., Irace A. and Mosca P. (2021) The Alps-Apennines Interference Zone: A Perspective from the Maritime and Western Ligurian Alps. *Geosciences*, **11**(5), 185.

Plunder A., Agard P., Dubacq B., Chopin C. and Bellanger M. (2012) How continuous and precise is the record of P–T paths? Insights from combined thermobarometry and thermodynamic modelling

into subduction dynamics (Schistes Lustrés, W. Alps). *Journal of Metamorphic Geology*, **30**(3), 323-346.

Polino R., Gosso G. and Dal Piaz G.V. (1990) Un modello attualistico sulla genesi delle Alpi. *Memorie della Società Geologica Italiana*, **45**, 71-75.

Pourteau A., Bousquet R., Vidal O., Plunder A., Duesterhoeft E., Candan O. and Oberhänsli R. (2014) Multistage growth of Fe–Mg–carpholite and Fe–Mg–chloritoid, from field evidence to thermodynamic modelling. *Contribution to Mineralogy and Petrology*, **168**, 1-25.

Powell R., Holland T.J.B.H. and Worley B. (1998) Calculating phase diagrams involving solid solutions via non-linear equations, with examples using THERMOCALC. *Journal of Metamorphic Geolology*, **16**(4), 577-588.

Powell R., Guiraud M. and White R.W. (2005) Truth and beauty in metamorphic phase-equilibria: conjugate variables and phase diagrams. *Canadian Mineralogist*, **43**(1), 21-33.

Regorda A., Spalla M. I., Roda M., Lardeaux J. M. and Marotta A. M. (2021). Metamorphic facies and deformation fabrics diagnostic of subduction: Insights from 2D numerical models. *Geochemistry, Geophysics, Geosystems*, *22*(10), e2021GC009899.

Roda M., Regorda A., Spalla M.I. and Marotta A.M. (2019) What drives A lpine T ethys opening? Clues from the review of geological data and model predictions. *Geological Journal*, **54**(4), 2646-2664.

https://doi.org/10.1180/mgm.2024.80 Published online by Cambridge University Press

Rosenbaum G., Lister G.S. and Duboz C. (2002) Reconstruction of the tectonic evolution of the western Mediterranean since the Oligocene. *Journal of Virtual Explorer*, **8**, (103809).

Rutter E.H. (1983) Pressure solution in nature, theory, and experiment. *Journal of Geological Society*. Lond. **140**, 725-740.

Sagri M. (1984) Litologia, stratimetria e sedimentologia delle torbiditi di piana di bacino del Flysch di San Remo (Cretaceo superiore, Liguria occidentale). *Memorie della Società Geologica Italiana*, **28**, 577-586.

Sanità E., Lardeaux M., Marroni M., Gosso G. and Pandolfi L. (2020) Structural relationships between Helminthoid Flysch and Briançonnais Units in the Marguareis Massif: A key for deciphering the finite strain pattern in the external southwestern Alps. *Geological Journal*, **56**(4), 2024-2040.

Sanità E., Lardeaux J.M., Marroni M., Gosso G. and Pandolfi L. (2021) Deciphering large-scale superposed fold systems at shallow crustal levels in collision zones: insights from the Marguareis Massif (southwestern Alps). *Journal of Maps*, **17**(2), 571-580.

Sanità E., Lardeaux J.M., Marroni M. and Pandolfi L. (2022a) Kinematics of the Helminthoid Flysch–Marguareis Unit tectonic coupling: consequences for the tectonic evolution of Western Ligurian Alps. *Comptes Rendue of Géoscience*, **354**(G1), 141-157

Sanità E., Di Rosa M., Lardeaux J.M., Marroni M. and Pandolfi L. (2022b) Metamorphic peak estimates of the Marguareis Unit (Briançonnais Domain): New constrains for the tectonic evolution of the south-western Alps. *Terra Nova*, **34**(4), 305-313.

https://doi.org/10.1180/mgm.2024.80 Published online by Cambridge University Press

Sanità E., Di Rosa M., Lardeaux J.M., Marroni M. and Pandolfi L. (2022c) The Moglio-Testico Unit (Ligurian Alps, Italy) as Subducted Metamorphic Oceanic Fragment: Stratigraphic, Structural and Metamorphic Constraints. *Minerals*, **12**(11), 1343.

Sanità E. (2023) *The complexity of shallow levels tectonics during continental collision: evidence from the boundary between Maritime and Ligurian Alps*. Dissertation. Università di Firenze.

Sanità E., Di Rosa M., Lardeaux J.M., Marroni M. and Pandolfi L. (2023) Tectonic coupling of oceanic and continental units in the Southwestern Alps (Western Liguria, Italy) revealed by structural mapping. *Journal of Maps*, **19**(1), 1-11.

Sassi F.P., Scolari A (1974) The b0 value of the potassic white micas as a barometric indicator in low-grade metamorphism of pelitic schists. *Contribution to Mineralogy and Petrology*, **45**(2), 143-152.

Scheffer C., Vanderhaeghe O., Lanari P., Tarantola A., Ponthus L., Photiades A. and France L. (2016) Syn-to post-orogenic exhumation of metamorphic nappes: Structure and thermobarometry of the western Attic-Cycladic metamorphic complex (Lavrion, Greece). *Journal of Geodynamics*, **96**, 174-193.

Schmid S.M., Fügenschuh B., Kissling E. and Schuster R. (2004) Tectonic map and overall architecture of the Alpine orogen. *Eclogae Geologicae Helvetie*, **97**, 93-117.

Schmid S.M., Kissling E., Diehl T., van Hinsbergen D.J. and Molli G. (2017) Ivrea mantle wedge, arc of the Western Alps, and kinematic evolution of the Alps–Apennines orogenic system. *Swiss Journal of Geoscience*, **110**, 581-612.

https://doi.org/10.1180/mgm.2024.80 Published online by Cambridge University Press

Seno S., Dallagiovanna G. and Vanossi M. (2003) Palaeogeography and thrust development in the Penninic domain of the Western Alpine chain: examples from the Ligurian Alps. *Bollletino della Società Geologica Italiana*, **122**(2), 223-232.

Seno S., Dallagiovanna G. and Vanossi M. (2005) A kinematic evolutionary model for the Penninic sector of the central Ligurian Alps. *International Journal of Earth Science*, **94**, 114-129.

Simon-Labric T., Rolland Y., Dumont T., Heymes T., Authemayou C., Corsini M. and Fornari M. (2009) 40Ar/39Ar dating of Penninic Front tectonic displacement (W Alps) during the Lower Oligocene (31-34 Ma). *Terra Nova*, **21**(2), 127-136.

Sinclair H.D. (1997) Tectonostratigraphic model for underfilled peripheral foreland basins: An Alpine perspective. *Geological Society of American Bulletin*, **109**(3), 324-346.

Syracuse E.M., van Keken P.E. and Abers G.A. (2010) The global range of subduction zone thermal models. *Phys Earth Planet Int*, **183**(1-2), 73-90.

Spear F.S., Pattison D.R. and Cheney J.T. (2016) The metamorphosis of metamorphic petrology.

Stampfli G.M., Borel G.D., Cavazza W., Mosar J. and Ziegler P.A. (2001) Palaeotectonic and palaeogeographic evolution of the western Tethys and PeriTethyan domain (IGCP Project 369). *Episodes*, **24**(4), 222-228.

Štípská P., Powell R., Hacker B.R., Holder R. and Kylander-Clark A.R.C. (2016) Uncoupled U/Pb and REE response in zircon during the transformation of eclogite to mafic and intermediate granulite (Blanský les, Bohemian Massif). *Journal of Metamorphic Geology*, **34**(6), 551-572.

https://doi.org/10.1180/mgm.2024.80 Published online by Cambridge University Press

Stöckhert B. and Gerya T. (2005) Pre-collisional high-pressure metamorphism and nappe tectonics at active continental margins: a numerical simulation. *Terra Nova* **17**, 102–110.

Strzerzynski P., Guillot S., Leloup P.H., Arnaud N., Vidal O., Ledru P., Corrioux G. and Darmendrail X. (2011) Tectono-metamorphic evolution of Brianconnains zone (Modane-Aussois and south- ern Vanoise units, Lyon Turin transect, Western Alps). *Journal of Geodynamics*, **56-57**, 55-75.

Tinkham D.K. and Ghent E.D. (2005) Estimating PT conditions of garnet growth with isochemical phase-diagram sections and the problem of effective bulk-composition. *Canadian Mineralogist*, **43**(1), 35-50.

Tracy R.J. (1982) Compositional zoning and inclusions in metamorphic minerals. *Review in Mineralogy and Geochemistry*, **10**, 355-397.

Tricart P., Schwartz S., Sue C., Poupeau G. and Lardeaux J.M. (2001) La denudation tectonique de la zone ultradauphinoise et l'inversion du front brianconnais au sud-est du Pelvoux (Alpes occidentales); une dynamique miocene a actuelle. *Bulletin de la Societé Géologique de la France*, **172**(1), 49-58.

Vanossi M., Cortesogno L., Galbiati B., Messiga B., Piccardo G. and Vannucci R. (1984) Geologia delle Alpi Liguri: dati, problemi, ipotesi. *Memorie della Società Geologica Italiana*, **28**, 5-75.

https://doi.org/10.1180/mgm.2024.80 Published online by Cambridge University Press

Verdecchia S.O., Collo G., Zandomeni P.S., Wunderlin C. and Fehrmann M. (2019) Crystallochemical indexes and geothermobarometric calculations as a multiproxy approach to PT condition of the low-grade metamorphism: The case of the San Luis Formation, Eastern Sierras Pampeanas of Argentina. *Lithos*, **324**, 385-401.

Vidal O., Goffé B. and Theye T. (1992) Experimental study of the stability of sudoite and magnesiocarpholite and calculation of a new petrogenetic grid for the system FeO–MgO–Al2O3–SiO2–H2O. *Journal of Metamorphic Geology*, **10**(5), 603-614.

Vidal O., Goffé B., Bousquet R. and Parra T. (1999) Calibration and testing of an empirical chloritoidchlorite Mg-Fe exchange thermometer and thermodynamic data for daphnite. *Journal of Metamorphic Geology*, **17**, 25-40.

Vidal O. and Parra T. (2000) Exhumation paths of high-pressure metapelites obtained from local equilibria for chlorite–phengite assemblages. *Geological Journal*, **35**(3-4), 139-161.

Vidal O., Parra T. and Trotet F. (2001) A thermodynamic model for Fe-Mg aluminous chlorite using data from phase equilibrium experiments and natural pelitic assemblages in the 100 to 600 C, 1 to 25 kb range. *American Journal of Sciences*, **301**(6), 557-592.

Vidal O., Parra T. and Vieillard P. (2005) Thermodynamic properties of the Tschermak solid solution in Fe-chlorite: Application to natural examples and possible role of oxidation. *American Mineralogist*, **90**(2-3), 347-358.

Vidal O., de Andrade V., Lewin E., Munoz M., Parra T. and Pascarelli S. (2006) P–T-deformation-Fe3+/Fe2+ mapping at the thin section scale and comparison with XANES mapping: application to a

https://doi.org/10.1180/mgm.2024.80 Published online by Cambridge University Press

garnet-bearing metapelite from the Sambagawa metamorphic belt (Japan). *Journal of Metamorphic Geology*, **24**(7), 669-683.

Zheng Y.F. and Chen Y.X. (2016) Continental versus oceanic subduction zones. *Nature Science Review*, **3**(4), 495-519.

Warr L.N. and Mählmann R.F. (2015) Recommendations for Kübler index standardization. *Clay Minerals*, **50**(3), 283-286.

Warr L.N. (2021) IMA–CNMNC approved mineral symbols. *Mineralogical Magazine*, **85**(3), 291-320.

Weaver C.E. (1961) in: *Clay minerals of the Ouachita structural belt and the adjacent foreland. In: Flaun PT Goldstcio* (Jr. King PB, Weaver CE Eds) The Ouachrro Belt., University of Texas Publication, pp 147-160

White R.W., Powell R. and Johnson T.E. (2014) The effect of Mn on mineral stability in metapelites revisited: New a–x relations for manganese-bearing minerals. *Journal of Metamorphic Geology*, **32**(8), 809-828.

Willner A. P. (2021) Very-low-grade metamorphism. *Encyclopedia of Geology*, *2*, 513-521.

https://doi.org/10.1180/mgm.2024.80 Published online by Cambridge University Press

Xiang H. and Connolly J.A. (2022) GeoPS: An interactive visual computing tool for thermodynamic modelling of phase equilibria. *Journal of Metamorphic Geology*, **40**(2), 243-255.

https://doi.org/10.1180/mgm.2024.80 Published online by Cambridge University Press

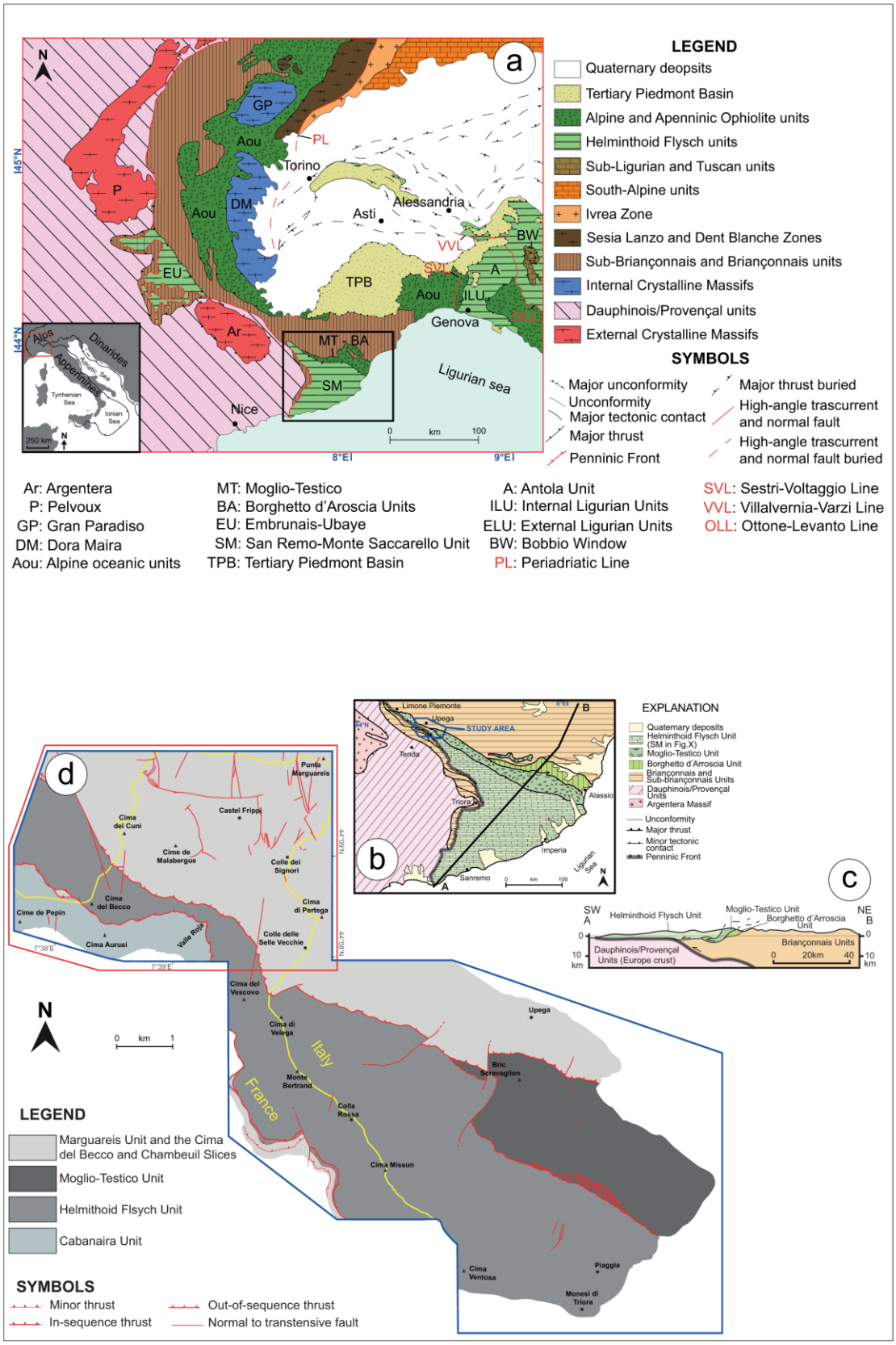

https://doi.org/10.1180/mgm.2024.80 Published online by Cambridge University Press

Fig. 1 a) Geological scheme of the Western Alps-Northern Apennines (modified and re-draw from Molli et al., 2010 and Sanità et al., 2020). b) Close-up of the Western Ligurian Alps (black box of a) with the related geological cross-section (c) modified by Bonini et al. (2010). d) Simplified geological sketch (blue box of b) of the boundary between Maritime and Ligurian Alps

https://doi.org/10.1180/mgm.2024.80 Published online by Cambridge University Press

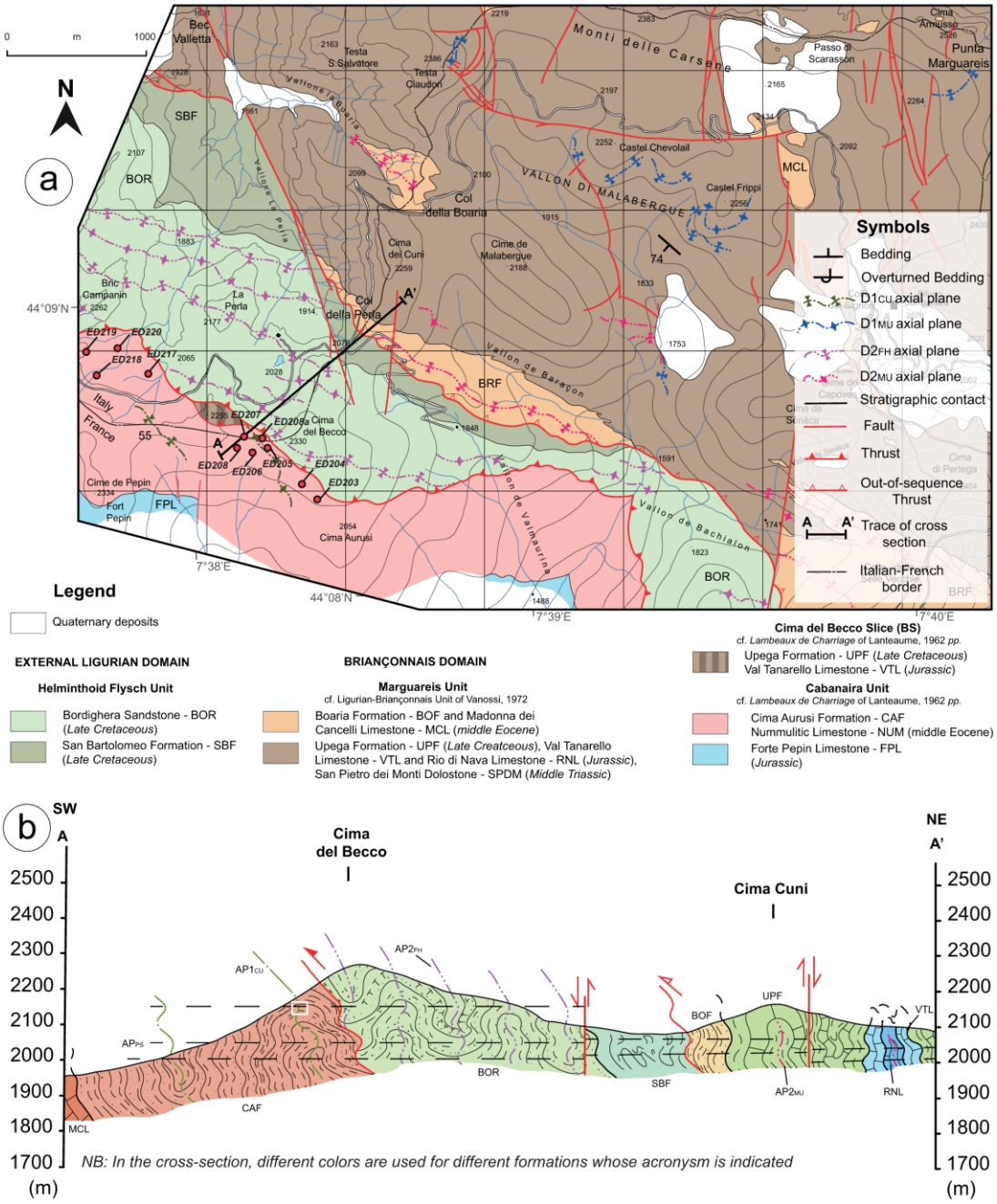

https://doi.org/10.1180/mgm.2024.80 Published online by Cambridge University Press

Fig. 2 a) Geological map (modified from Sanità et al., 2020 and 2021) of the Marguareis Massif (red box of Figure 1d) with the related geological cross-section (b). In the map the locations of samples are reported (red dots).

https://doi.org/10.1180/mgm.2024.80 Published online by Cambridge University Press

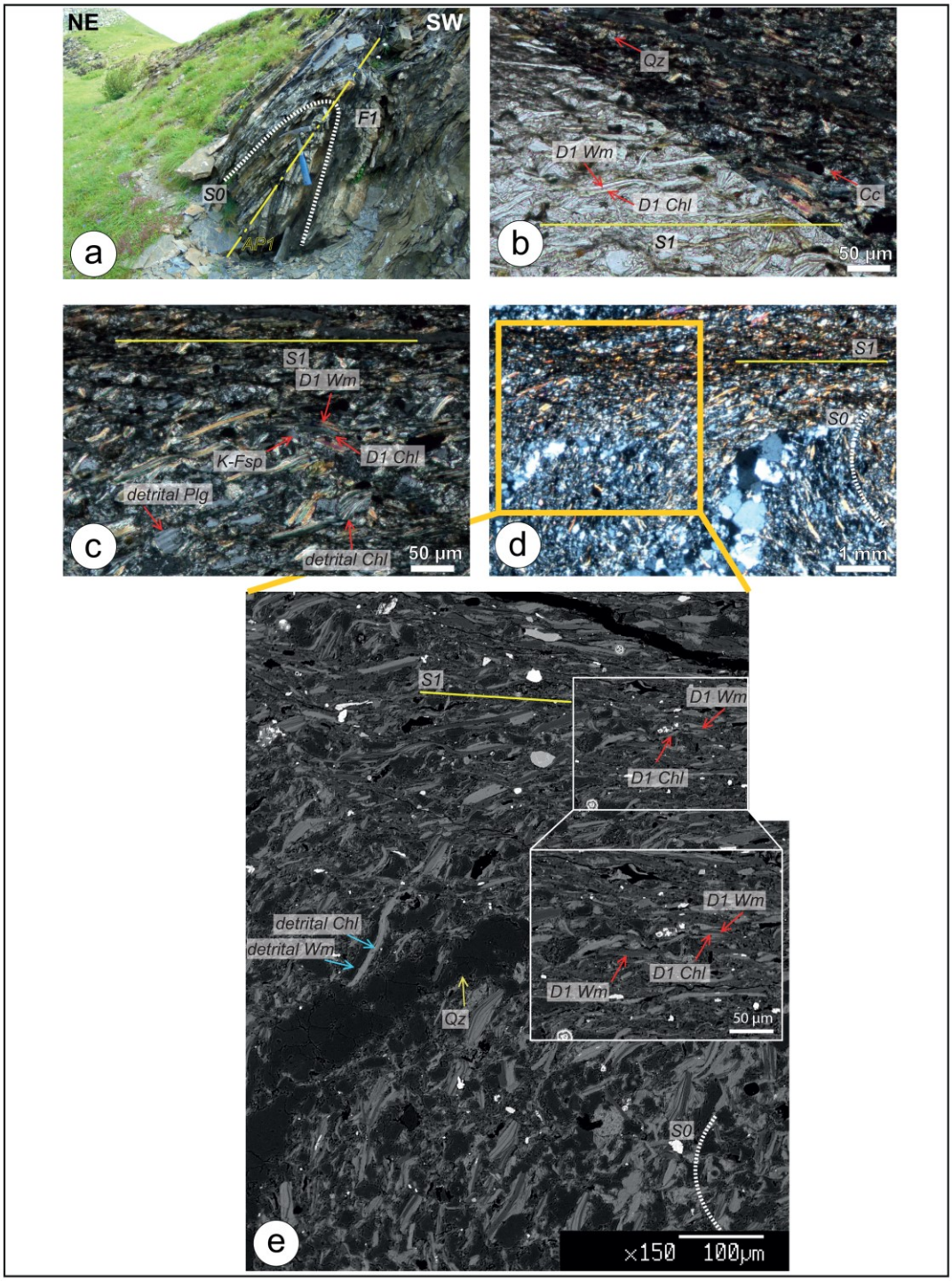

https://doi.org/10.1180/mgm.2024.80 Published online by Cambridge University Press

Fig. 3 Macro- to micro-scale D1 phase-related structural features. a) F1 fold system in the Cabanaira Unit (white box of Figure 2b). b, c) S1 (yellow line) slaty cleavage (bottom left of b: plane polarized light, top right of b and c: crossed polarized light) marked by syn metamorphic Wm and Chl and Qz in textural equilibrium. Detrital grains of Plagioclase and chlorite (c) can be observed. d) Microphotograph of F1 hinge-zone where clear cross-cutting relationships between S1 (yellow line) and bedding (S0, white dashed line) are shown. e) BSE image of the micro-area investigated to perform the *P–T* estimates (orange box of d). The white box represents the area where the local bulk composition was extracted to perform forward and inverse thermodynamic modelling. Along the S0 (white dashed line), detrital Wm and Chl (blue arrows) are indicates. Along the S1 (yellow line) neo-formed Wm and Chl crystals (red arrows in the white boxes) are present

https://doi.org/10.1180/mgm.2024.80 Published online by Cambridge University Press

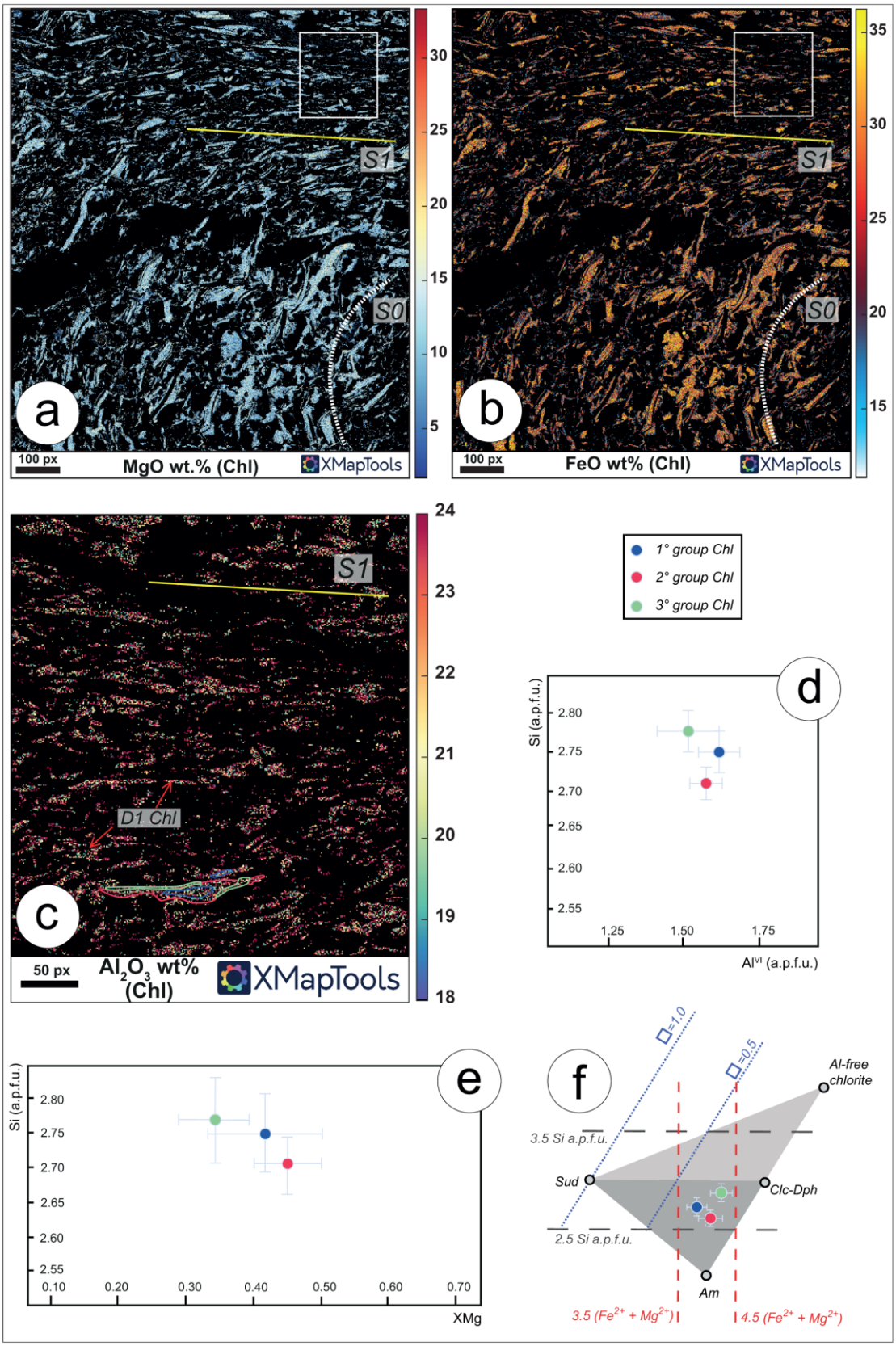

https://doi.org/10.1180/mgm.2024.80 Published online by Cambridge University Press

Fig. 4 Mineral chemistry of chlorites in ED208a sample. MgO wt.% (a) and FeO wt.% variation in the microdomain signaled in Figure 3e. Differences exist between detrital (white dotted line) and syn-metamorphic (yellow line) Chl grains. c) Enlarged area of the white box of (a) and (b) of the syn-metamorphic Chl (red arrows) grew along the S1 foliation (yellow line). The Al_2O_3 wt.% variation sheds light the complex mineral chemistry of the neo-formed grains (blue, red and green areas) corresponding to first, second and third groups (see the text). d) Al^{VI}/Si and (e) XMg/Si plots referred to the average compositions of the three groups of Chl detected along the S1 foliation are reported with their error bars. f) Octhedral Fe^{2+} + Mg^{2+} (red dashed lines) content vs. Si (grey dashed lines) diagram (according with Bourdelle and Cathelineau, 2015). The blue dotted lines show the octahedral vacancy (blue empty squares) values. The four Chl end-members are also reported.

https://doi.org/10.1180/mgm.2024.80 Published online by Cambridge University Press

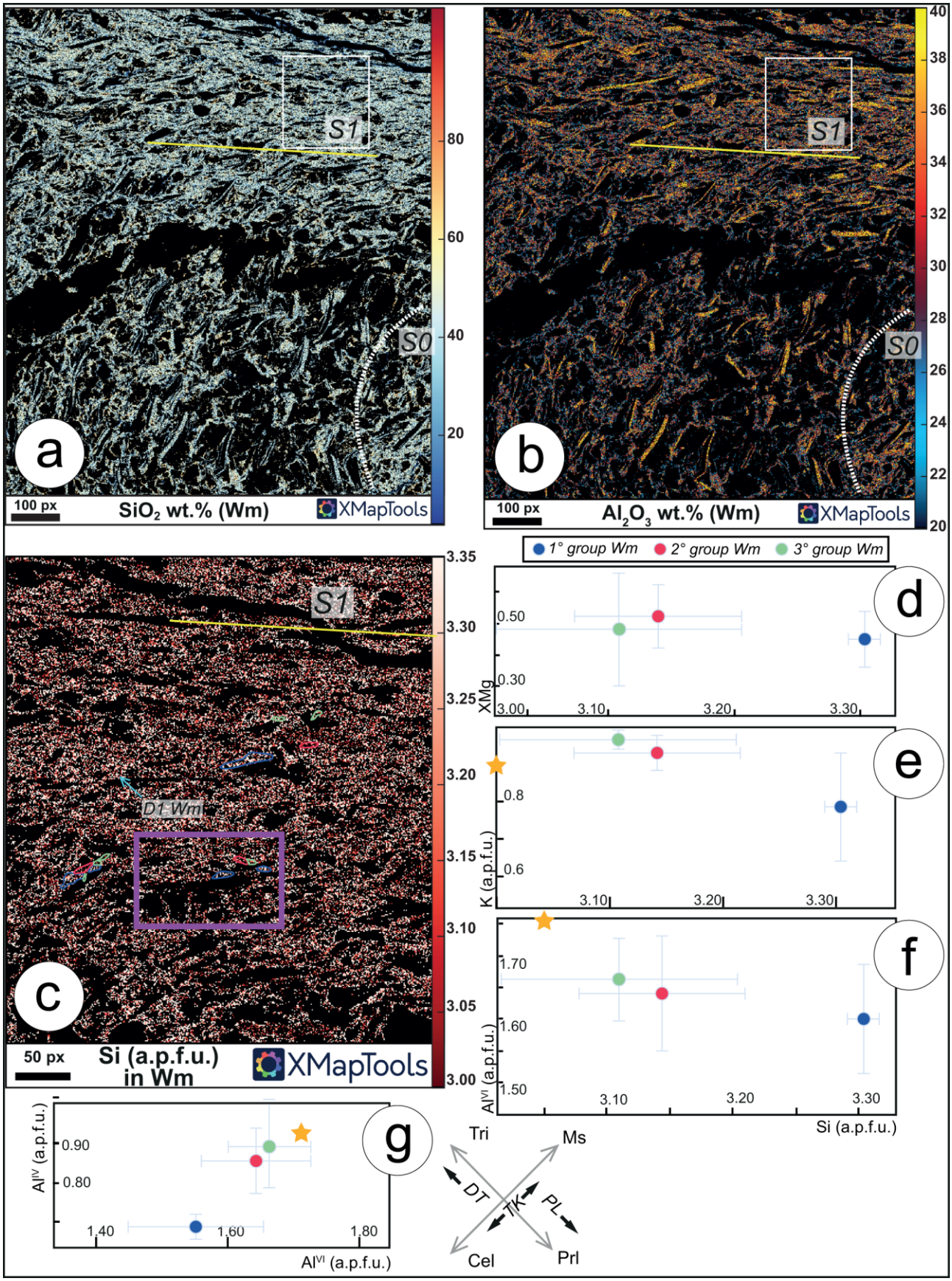

https://doi.org/10.1180/mgm.2024.80 Published online by Cambridge University Press

Fig 5 Mineral chemistry of Wm in ED208a sample. SiO_2 wt.% (a) and Al_2O_3 wt.% variation in the microdomain of Figure 3e. Differences exist between detrital (white dotted line) and syn-metamorphic (yellow line) Wm grains. c) Enlarged area of the white box of (a) and (b) of the syn-metamorphic Wm (light blue arrow) grew along the S1 foliation (yellow line). The Si content variation outlines a complex mineral chemistry of the syn-metamorphic Wm (blue, red and green areas) corresponding to first, second and third groups (see the text). The purple box indicates the Chl the location of chlorite crystal shown in the Figure 4c. XMg/Si (d), K/Si and (e) Al^{VI}/Si (f) plots referred to the average composition of the three groups of Wm detected along the S1 foliation are indicate with the related error bars. The orange stars indicate theoretical compositional of muscovite. g) Al^{IV}/Al^{VI} plot (according with Bousquet et al., 2002). The grey arrows indicate the solid solution trend of Wm, while the black arrows indicate the main substitution (TK: Tschermak; DT: di-trioctahedral; PL: Pyrophyllitic).

https://doi.org/10.1180/mgm.2024.80 Published online by Cambridge University Press

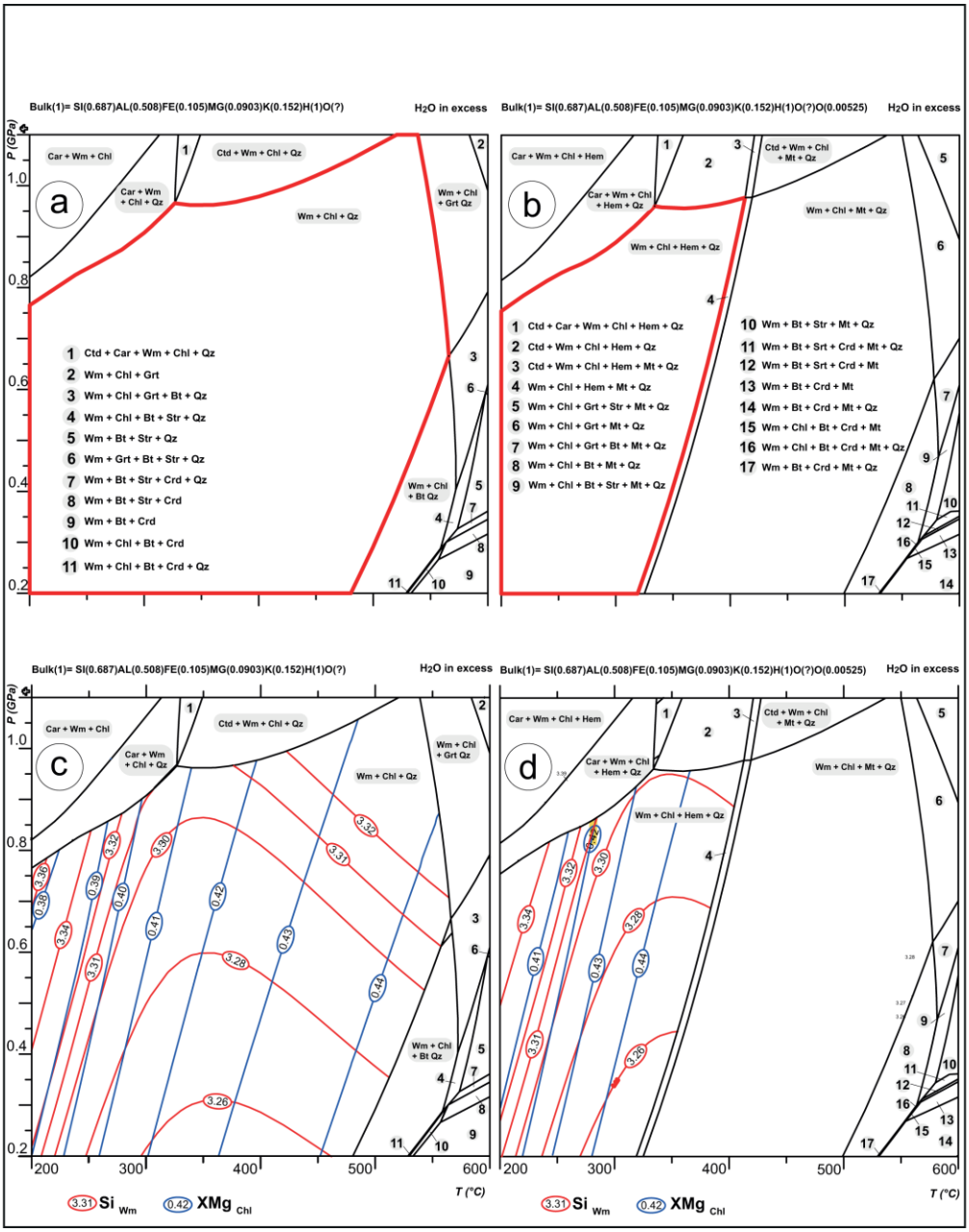

Fig 6 Isochemical phase diagrams related to the micro-domain within the white box of Figure 3e. a) Phase diagram with $FeO_{TOT}=Fe^{2+}$. b) Phase diagram where 10% of FeOtot=Fe^{3+}. Black lines mark the boundary between different stability field, whereas the red ones indicate the field where the observed mineral assemblage is found to be stable. c, d) Isochemical phase diagrams contoured for Si (Wm) and XMg (Chl) isopleths. The LBC is reported in moles of elements at the top of the diagrams. In the grey boxes, the stable mineral assemblages relate to the different fields are indicated. The yellow area indicates the *P/T* space of (d) in which the measured value of Si and XMg (for Wm and Chl, respectively) match with that predicted by the model. At the bottom of each diagram, the

https://doi.org/10.1180/mgm.2024.80 Published online by Cambridge University Press

contour legend is reported and the numbers inside the ellipses represents values of the related observed isopleth. Car: Carpholite; Ctd: Chloritoid; Grt: Garnet; Bt: Biotite; St: Staurolite; Crd: Cordierite; Hem: Hematite; Mt: Magnetite

https://doi.org/10.1180/mgm.2024.80 Published online by Cambridge University Press

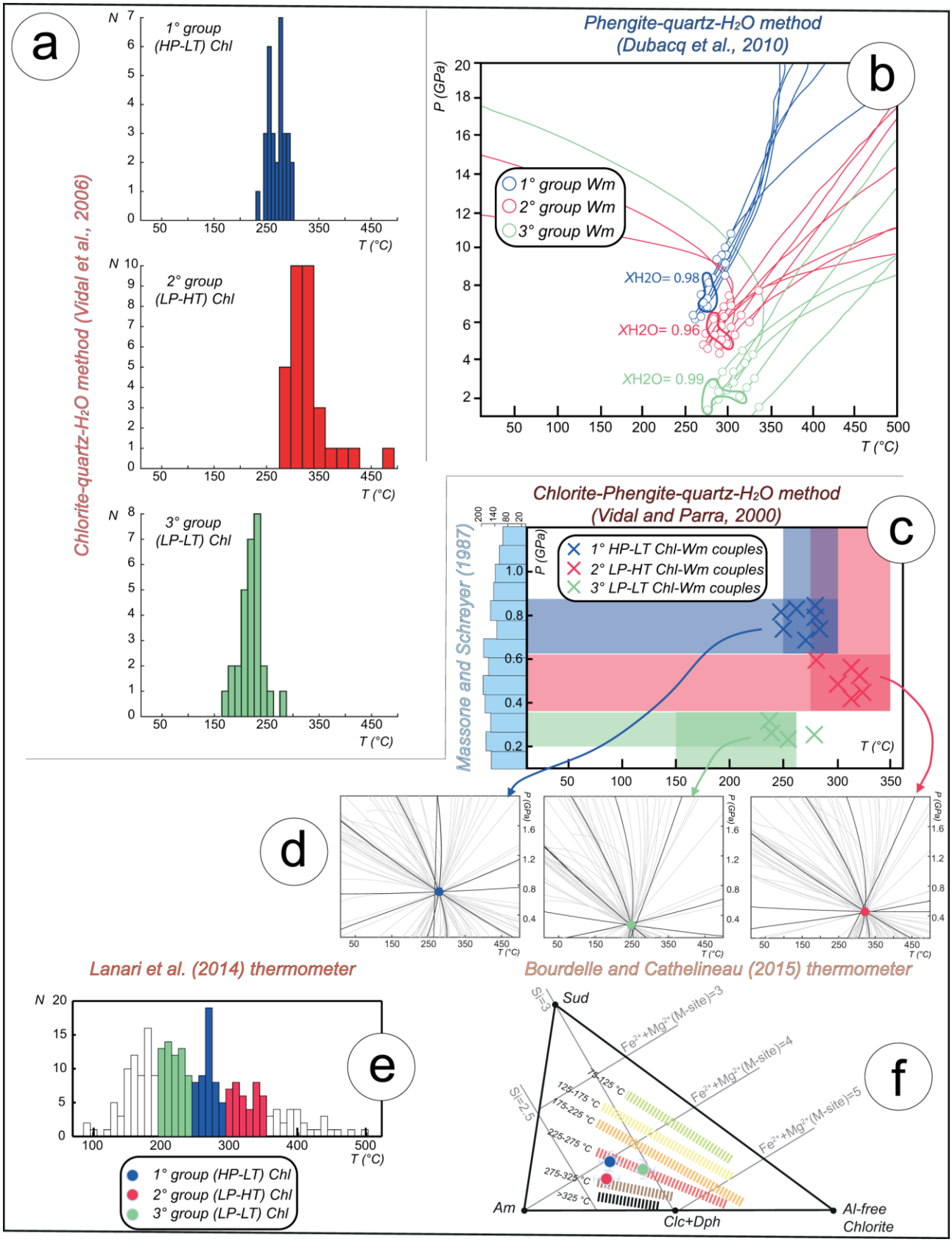

Fig 7 *P–T* estimates results. a) Histograms of temperature range of Chl formation belonging to the three groups obtained with the Chl-Qz-H_2O. Each bar represents the counts of each chlorite whose

https://doi.org/10.1180/mgm.2024.80 Published online by Cambridge University Press

temperature formation falls in a specific range reported along the X-axis. b) Results of Phg-Qz-H_2O barometer; within the *P/T* space the equilibrium lines Wm+Qz+H_2O, along with only the hydration state (empty circles along each line) of white mica changes, are reported for each Wm groups. The XH_2O values used in the model for each Wm group are also indicate. c) *P/T* diagram showing the results of *P–T* estimates from the Chl-Phg-Qz-H_2O method. Each cross indicates the pressure and temperature equilibrium condition for a single Chl-Wm couple belonging to the first, the second and the third groups. The blue, red and green boxes mark the temperature and pressure ranges of Chl and Wm formations obtained with the methods reported in a and b. Along the Y-axis, the histogram shows the results of Massone and Schreyer (1987) barometer. Each bar represents the counting of pressure values for each pixel inside the micro-domain of Figure 3e. d) *P/T* space showing examples of all the independent (black lines) and dependent (grey lines) equilibria obtained with the Chl-Phg-Qz-H_2O for each Chl-Wm couple belonging to the first, the second and the third group. e) Histograms showing the results of Lanari et al. (2014) geothermometer. Each bar statistically represents temperature range values of chlorite formation. f) Diagram showing the results of Bourdelle and Cathelineau (2015) geothermometer, where the dashed lines indicate different *T* ranges. Here, the plot of each average values referred to the different groups of chlorite are reported with their error bars.

https://doi.org/10.1180/mgm.2024.80 Published online by Cambridge University Press

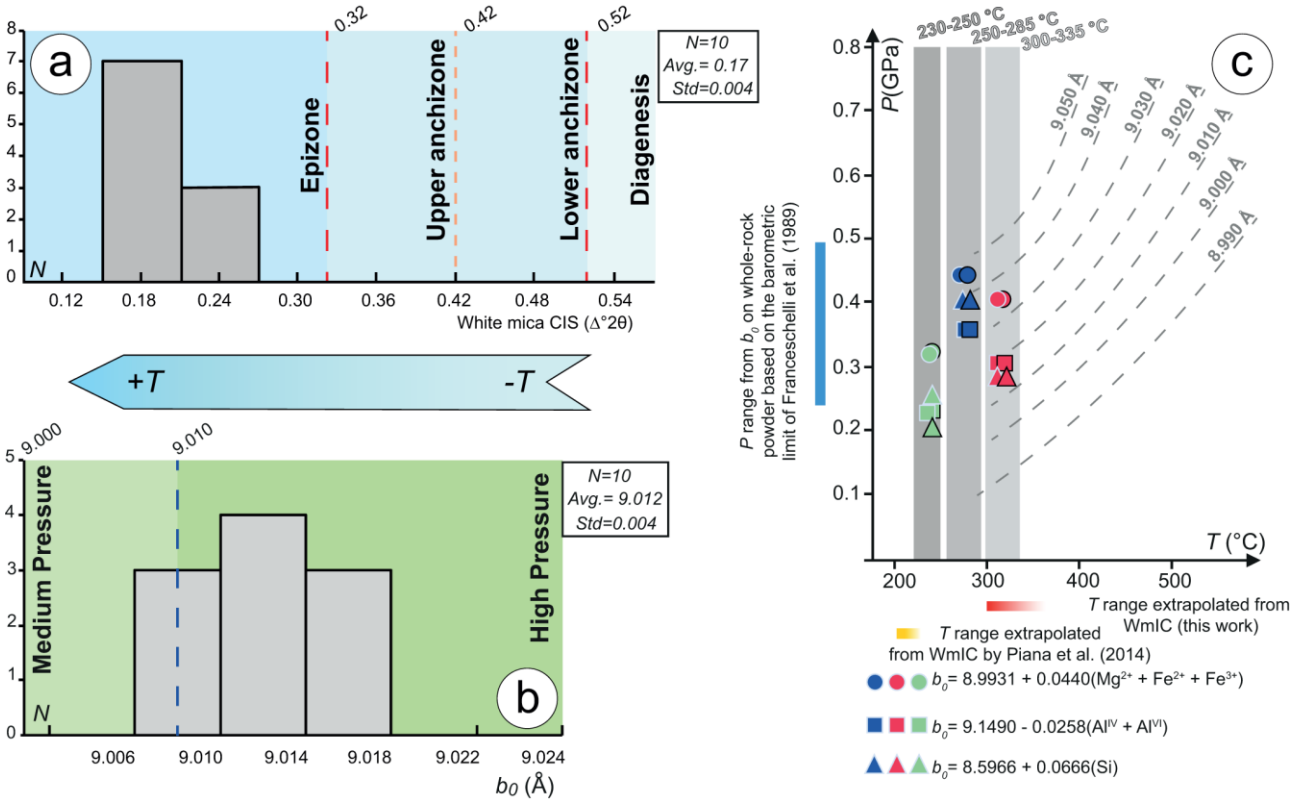

Fig. 8 Crystallochemical indexes distribution. a) WmIC distribution. b) b_0 cell parameters distribution from XRD patterns. c) b_0 values calculated using the Verdecchia et al. (2019) spreadsheet. The grey rectangular boxes represent the three *T* ranges independently obtained with thermobaric methods. Along Y- and X-axes the cystallochemical index distribution (colored rectangular bars) obtained using the XRD patterns analysis is reported. The *T* ranges calculated by Piana et al. (2014) is reported (yellow rectangular bar along the X-axis). The shaded effect indicates that the upper limit of the range is poorly constrained with this method. The triangles, circles and squares contoured in black are referred to calculation in which 10% of ferric iron is considered.

https://doi.org/10.1180/mgm.2024.80 Published online by Cambridge University Press

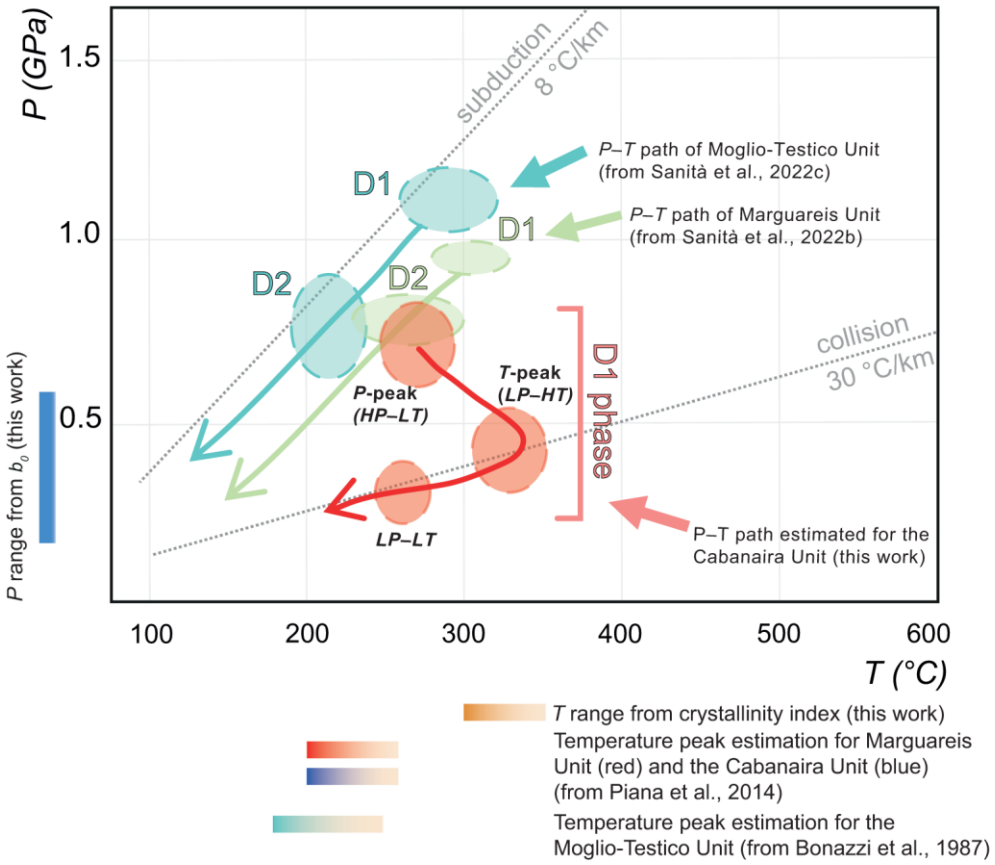

Fig. 9 Diagram showing the *P–T* path of the Cabanaira Unit constrained in this work. The paths estimated for the Marguareis and Moglio-Testico Unit are also represented (data from Sanità et al., 2022b; 2022c). The geothermal gradients typical of subduction and collision setting are also shown. Along the X-axis the *T* ranges extrapolated by means Illite crystallinity Index for the Marguareis (red rectangular bar data from Piana et al., 2014), Cabanaira (blue rectangular bar from Piana et al., 2014; orange rectangular bar from this work) and the Moglio-Testico (light blue rectangular bar from Bonazzi et al., 1987) Units are reported. The shaded effect indicates that the upper limit of the range is poorly constrained with this method. Along the Y-axis the *P* range yielded from b_0 measurement (this work) are reported. The length of rectangular boxes represents the range of temperature and pressure estimates.

https://doi.org/10.1180/mgm.2024.80 Published online by Cambridge University Press

Table 1. Average compositions (wt.%) related to the three groups of Chl Standard deviation is indicated.

	1° group Chl*		2° group Chl*		3° group Chl*	
SiO_2	25.85	±2.21	25.85	±2.79	25.85	±1.24
TiO_2	< 0.01		0.12	±0.10	< 0.01	
Al_2O_3	22.99	±0.56	23.27	±0.40	2.,87	±2.38
FeO	27.19	±2.27	26.05	±1.60	31.72	±3.20
MnO	0.04	±0.04	0.06	±0.03	0.08	±0.00
MgO	10.89	±2.50	12.08	±1.77	9.17	±1.18
CaO	0.17	±0.07	0.17	±0.05	0.09	±0.04
Na_2O	< 0.01		< 0.01		< 0.01	
K_2O	0.34	±0.34	0.21	±0.24	0.17	±0.08
Total	88.66	±1.18	89.21	±0.83	88.94	±0.39
Si	2.75	±0.06	2.72	±0.04	2.77	±0.07
Al^{IV}	1.25	±0.06	1.28	±0.04	1.23	±0.07
Al^{VI}	1.63	±0.06	1.60	±0.04	1.52	±0.16
Ti	-		0.00	±0.01	0.00	
Fe_{TOT}	2.42	±0.26	2.29	±0.18	2.84	±0.36
Mn	0.00	±0.00	0.01	±0.00	0.01	±0.00
Mg	1.73	±0.36	1.89	±0.25	1.46	±0.15
Ca	0.02	±0.00	0.02	±0.01	0.01	±0.00
Na	n.d.		n.d.		n.d.	
K	0.05	±0.05	0.03	±0.02	0.02	±0.00
M-site	5.79	±0.04	5.79	±0.03	5.83	±0.05
sum cations	9.85	±0.85	9.88	±0.59	9.87	±0.81
vacancy	0.19	±0.06	0.16	±0.04	0.15	±0.04
XMg	0.42	±0.08	0.45	±0.05	0.34	±0.05
Clin + Daph	0.53	±0.03	0.50	±0.02	0.59	±0.12
Am	0.28	±0.09	0.34	±0.06	0.26	±0.07
Sud	0.19	±0.06	0.16	±0.04	0.15	±0.04

* average and standard deviation were obtained from 50 analysis for group from XMapTools.

https://doi.org/10.1180/mgm.2024.80 Published online by Cambridge University Press

Table 2. Average compositions related to the three groups of Wm. Standard deviation is indicated.

	1° group Wm*		2° group Wm*		3° group Wm*	
SiO_2	48.61	±2.03	45.68	±3.51	46.56	±1.24
TiO_2	0.14	±0.07	0.00	±0.00	0.27	±0.18
Al_2O_3	28.13	±3.16	31.05	±3.16	32.33	±2.33
FeO	5.72	±1.17	4.04	±2.67	4.04	±1.43
MnO	0.02	±0.00	0.01	±0.01	< 0.01	
MgO	2.71	±0.58	2.38	±1.47	2.04	±0.72
CaO	0.02	±0.02	0.27	±0.38	0.02	±0.02
Na_2O	< 0.01		< 0.01		< 0.01	
K_2O	9.03	±3.13	10.61	±1.03	11.51	±0.01
Total	94.25	±2.63	94.03	±5.48	96.76	±0.03
Si	3.31	±0.02	3.14	±0.08	3.11	±0.10
Al^{IV}	0.69	±0.02	0.86	±0.08	0.89	±0.10
Al^{VI}	1.56	±0.10	1.64	±0.09	1.66	±0.07
Ti	0.01	n.d.	n.d.	n.d.	0.01	n.d.
Fe_{TOT}	0.32	±0.07	0.24	±0.18	0.23	±0.08
Mn	n.d.	n.d.	n.d.	n.d.	n.d.	
Mg	0.28	±0.08	0.24	±0.14	0.20	±0.07
Ca	n.d.	n.d.	0.02	±0.01	n.d.	n.d.
Na	n.d.		n.d.		n.d.	
K	0.79	±0.30	0.93	±0.03	0.98	±0.01
A site	0.79	±0.30	0.95	±0.05	0.98	±0.01
M-site	2.17	±0.08	2.13	±0.11	2.11	±0.04
sum cations	2.96	±0.33	3.07	±0.16	3.09	±0.05
vacancy	0.20	±0.15	0.05	±0.05	0.02	±0.01
XMg	0.46	±0.10	0.52	±0.22	0.48	±0.18
Ms	0.52	±0.09	0.73	±0.06	0.77	±0.08
Cel	0.20	±0.15	0.16	±0.13	0.11	±0.13
Prl	0.20	±0.12	0.08	±0.01	0.02	±0.01
Trioct.	0.17	±0.08	0.13	±0.11	0.11	±0.04

* average and standard deviation were obtained from 50 analysis for group from XMapTools.

https://doi.org/10.1180/mgm.2024.80 Published online by Cambridge University Press